RNA G-quadruplexes forming scaffolds for α-synuclein aggregation lead to progressive neurodegeneration

Kazuya Matsuo[1], Sefan Asamitsu[1,2], Kohei Maeda[1,3], Kosuke Kawakubo[1,3], Ginji Komiya[1,3], Kenta Kudo[1,3], Yusuke Sakai[1,3], Karin Hori[1], Susumu Ikenoshita[1,4], Shingo Usuki[5], Shiori Funahashi[6], Yasushi Kawata[6], Tomohiro Mizobata[6], Norifumi Shioda[1,3]* and Yasushi Yabuki[1,3]*

1. Department of Genomic Neurology, Institute of Molecular Embryology and Genetics (IMEG), Kumamoto University, Kumamoto, Japan
2. Center for Biosystems Dynamics Research (BDR), RIKEN, Kobe, Japan
3. Graduate School of Pharmaceutical Sciences, Kumamoto University, Kumamoto, Japan.
4. Department of Neurology, Graduate School of Medical Sciences, Kumamoto University, Kumamoto, Japan.
5. Liaison Laboratory Research Promotion Center, Institute of Molecular Embryology and Genetics (IMEG), Kumamoto University, Kumamoto, Japan.
6. Department of Chemistry and Biotechnology, Graduate School of Engineering Tottori University, Tottori, Japan

*Correspondence should be addressed to Norifumi Shioda and Yasushi Yabuki

Norifumi Shioda
Department of Genomic Neurology, Institute of Molecular Embryology and Genetics, Kumamoto University, 2-2-1 Honjo, Chuo-ku, Kumamoto 860-0811, Japan.
Tel: 81-96-373-6633
E-mail: shioda@kumamoto-u.ac.jp

Yasushi Yabuki
Department of Genomic Neurology, Institute of Molecular Embryology and Genetics, Kumamoto University, 2-2-1 Honjo, Chuo-ku, Kumamoto 860-0811, Japan.
Tel: 81-96-373-6633
E-mail: yabukiy@kumamoto-u.ac.jp

Abstract

Synucleinopathies, including Parkinson's disease, dementia with Lewy bodies, and multiple system atrophy, are primarily neurodegenerative diseases with progressive decline in motor function[1,2,3,4,5,6]. Aggregates composed of α-synuclein, which are known as Lewy bodies, are a neuropathological hallmark of synucleinopathies; their pathogenesis has been attributed to neuronal loss owing to intracellular α-synuclein accumulation [1,2,3,7,8]. However, the mechanism of α-synuclein aggregation remains unclear. Here we show that the RNA G-quadruplexes assembly forms scaffolds for α-synuclein aggregation, thereby contributing to neurodegeneration. RNA G-quadruplexes undergo phase separation and form scaffolds for co-aggregation with α-synuclein. Upon pathogenic α-synuclein seeds-induced cellular stress and an optogenetic assembly of RNA G-quadruplexes, phase-separated RNA G-quadruplexes served as scaffolds for α-synuclein phase transition, and the co-aggregates initiated synaptic dysfunction and Parkinsonism in mice. Treatment with 5-aminolevulinic acid and protoporphyrin IX, which prevents RNA G-quadruplexes phase separation[9], attenuates α-synuclein phase transition, neurodegeneration, and motor deficits in synucleinopathy model mice. Together, the RNA G-quadruplexes assembly accelerates α-synuclein phase transition and aggregation owing to intracellular Ca^{2+} homeostasis, thereby contributing to the pathogenesis of synucleinopathies.

Main

α-synuclein (αSyn) is an intrinsically disordered protein (IDP) of 140 amino acids[10]. A relatively high concentration of αSyn is present in synaptic vesicle membranes; it is also present as a natively unfolded monomer in the cytoplasm[11]. Although the physiological role of αSyn remains elusive, it is presumably involved in synaptic vesicle clustering, docking, fusion, and recycling[12]. In pathological conditions, monomeric αSyn assembles into toxic oligomers, protofibrils, and amyloid-like fibrils in synucleinopathies, such as Parkinson's disease (PD), dementia with Lewy bodies (DLB), and multiple system atrophy (MSA)[1,2,3,4,5,6]. The aggregates composed of αSyn, which are known as Lewy bodies (LBs), are a neuropathological hallmark of synucleinopathies, and their pathogenesis has been attributed to neuronal loss[1,2,3,7,8]. However, the mechanism underlying the transformation of native αSyn into pathological aggregates is not completely understood.

Liquid–liquid phase separation (LLPS) represents a ubiquitous phenomenon in which molecules transition from a homogeneous state into a dense phase with different physiochemical properties (e.g., molecular crowding), inducing the formation of liquid droplets, hydrogels, and aggregates[13,14,15,16,17]. Proteins and RNAs often undergo LLPS due to multivalent macromolecular interactions with themselves and other biomolecules[9,13,18]. LLPS results in the formation of membraneless ribonucleoprotein (RNP) organelles enriched in RNA and RNA-binding proteins (RBPs), including nucleoli, Cajal bodies, nuclear speckles, stress granules (SGs), processing bodies (P-bodies), and neuronal RNA granules[19,20]. The liquid–solid phase transition via LLPS could be an important intermediate step for aggregate formation in neurodegenerative disease-associated IDPs, such as αSyn[21], tau[22], fused in sarcoma (FUS)[23], TAR DNA-binding Protein of 43 kDa (TDP-43)[24], and heterogeneous nuclear ribonucleoprotein A1 (hnRNP A1)[25], whereas the intrinsic factor that facilitates the phase transition has not been identified.

We found that RNA G-quadruplexes (rG4s), which are quadruple-stranded structures formed by contiguous guanines[26], bind to αSyn and induce aggregation. rG4 itself undergoes LLPS in a Ca^{2+}-dependent manner, acting as a scaffold for αSyn aggregation. In αSyn pre-formed fibrils (PFFs)-treated mouse neurons forming LB-like inclusions similar to human synucleinopathies[27,28], αSyn co-aggregated with rG4 assembly consisting of synaptic mRNAs associated with intracellular Ca^{2+} overload, thereby demonstrating synaptic dysfunction. In pharmacological experiments, oral administration of 5-aminolevulinic acid (5-ALA), which intracellularly generates protoporphyrin IX (PPIX) that inhibits rG4s LLPS[9,29], suppressed αSyn aggregation and

92 improved behavioral motor deficits in αSyn PFF-treated mice. These results provide
93 evidence that rG4s assembly induces sol–gel phase transition of αSyn, eliciting
94 progressive neurodegeneration.
95
96 **αSyn binds to rG4s and undergoes sol–gel phase transition**
97 First, we analyzed the temporal changes in the aggregation of endogenous αSyn
98 using primary mouse cortical neurons treated with human αSyn PFF. In untreated controls,
99 αSyn was found to be intracellularly diffuse assembling at synaptophysin-positive
100 presynapses along microtubule-associated protein 2 (MAP2)-positive neurites (**Extended**
101 **Data Fig. 1a**). However, after PFF treatment, αSyn showed significantly higher
102 inhomogeneity in the cytoplasm, existing as granules (**Fig. 1a, b**). The immunoreactivity
103 of αSyn phosphorylated at serine 129 (pS129), a central feature of the LB inclusion,
104 increased in a time-dependent manner and was evident eight days after PFF treatment
105 (**Fig. 1b** and **Extended Data Fig. 1b**). Of note, αSyn granules mainly co-localized with
106 decapping mRNA 1A (Dcp1a)-positive P-bodies (43.0%) but rarely with fragile X mental
107 retardation protein (FMRP)-positive RNA granules (3.2%) or p62-positive aggresomes
108 (18.9%) four days after the treatment (**Fig. 1a, b** and **Extended Data Fig. 1c**). However,
109 αSyn granules localized primarily in the aggresomes (43.9%) but rarely in the P-bodies
110 (6.1%) or the RNA granules (3.1%) eight days after the treatment (**Fig. 1a, b** and
111 **Extended Data Fig. 1c**). Since human antigen R (HuR)-positive SGs were not detected
112 upon PFF treatment (**Extended Data Fig. 1c**), neurons were treated with sodium arsenite
113 for SG formation. Although both HuR-positive SGs as well as αSyn granules were
114 detected in the cytoplasm after the treatment, they did not co-localize (**Extended Data**
115 **Fig. 1d**).
116 To assess the dynamic nature of αSyn with PFF treatment in cells, we utilized
117 HEK293 cells overexpressing green fluorescent protein (GFP)-tagged αSyn in the present
118 study. The GFP-tagged αSyn granules exhibited rapid recovery kinetics 24 h after PFF
119 treatment in fluorescence recovery after photobleaching (FRAP) assay (**Fig. 1c**,
120 **Extended Data Fig. 1e** and **Supplementary Video**), and the GFP-tagged αSyn granules
121 were not co-localized with pS129 or p62 (**Extended Data Fig. 1f**). However, the
122 fluorescence recovery was markedly reduced and αSyn granules co-localized with pS129
123 and p62 48 h after the treatment (**Fig. 1c**, **Extended Data Fig. 1e, f** and **Supplementary**
124 **Video**). These results suggest that αSyn transiently forms granules with RNPs via LLPS,
125 subsequently forming aggregates contributing to the pathogenesis of synucleinopathies.
126 Thereafter, we employed clustered regularly interspaced short palindromic repeats/Cas9
127 technology in several human cell lines (HEK293, Hela, and Hutu-80 cells) for

128 endogenous tagging with mNeonGreen at *SNCA* loci to reveal the dynamic nature of
129 endogenous αSyn with PFF treatment; however, both the N- and C-terminal tagging was
130 unsuccessful owing to unexplained cell death.

131 Since our data suggested that RNP granules containing RNAs and/or proteins
132 provide scaffolds for initial αSyn aggregation, we subsequently examined whether the
133 addition of cell-derived RNAs or proteins undergo sol–gel phase transition of αSyn *in*
134 *vitro*. Purified αSyn (69 μM) underwent LLPS according to the concentration of
135 polyethylene glycol (PEG), a molecular crowding agent, whereas no droplet formation
136 was observed without PEG (**Extended Data Fig. 2a**). Thereafter, we examined whether
137 RNAs impact αSyn LLPS by adding total RNAs extracted from Neuro-2a cells. RNA
138 addition decreased the PEG concentration required for αSyn LLPS and elicited a
139 transition from a droplet to a gel-like state (**Fig. 1d**). Fluorescence imaging studies using
140 mCherry-tagged αSyn (mCh-αSyn) confirmed that these gel-like aggregates contain αSyn
141 (**Fig. 1d**). In FRAP experiments in the presence of RNAs, the fluorescence recovery of
142 αSyn was faster in the droplets but not in the gel-like states (**Fig. 1e**). Similar experiments
143 were performed with nuclease-treated proteins: αSyn droplets formed in the presence of
144 PEG; however, no transition to a gel-like state occurred (**Extended Data Fig. 2b**).

145 These observations motivated us to examine the nucleotide-binding capacity of
146 αSyn and its sequence; therefore, we subsequently performed RNA Bind-n-Seq[30] using
147 recombinant human αSyn and a pool of random 24-nt RNA oligonucleotides *in vitro* (**Fig.**
148 **1f**). The top 10 αSyn binding RNA motifs were significantly guanine-rich sequences
149 (**Extended Data Fig. 3a–e** and **Supplementary Table 1**). Several runs at different
150 concentrations of αSyn revealed that these motifs require guanines in a contiguous but
151 not random sequence, thereby suggesting rG4s as a potential structure for αSyn binding
152 (**Fig. 1f** and **Extended Data Fig. 3f, g**). To investigate whether αSyn preferentially
153 interacts with rG4s, we performed an electrophoresis mobility shift assay (EMSA) using
154 various RNA oligonucleotide structures: G4tr—a typical rG4, telomeric repeat-
155 containing RNA (TERRA) $(UUAGGG)_4$ repeats, G4mt—a TERRA mutant that is unable
156 to form rG4 $(UUACCG)_4$ repeats, a hairpin structure—$(CAG)_8$ repeats, and polyA—
157 single-stranded and non-structured $(AAA)_8$ repeats (**Extended Data Fig. 4a**). αSyn
158 demonstrated high affinity only for G4tr and little or no affinity for other RNA structures
159 (**Fig. 1g** and **Extended Data Fig. 4b**). In quantitative surface plasmon resonance (SPR)
160 binding analysis, αSyn demonstrated much higher selectivity for G4tr (K_D = 3.63 ± 0.63
161 μM) compared to that with G4mt (K_D = n.d.) (**Fig. 1h** and **Extended Data Fig. 4c, d**).
162 αSyn is defined by three regions: 1) the N-terminal region (Nterm; residues 1–60), which
163 is basic and composed of seven imperfect repeats of 11 amino acids that contain a 4-

residue core with the consensus sequence KTKEGV; 2) the non-amyloid-β component region (NAC; residues 61–95), which is hydrophobic and forms the core of the fiber during aggregation; and 3) the C-terminus (Cterm; residues 96–140), which is a highly negatively charged region that binds to metal ions[31]. To identify the domains responsible for rG4-binding capability, we constructed three mutant αSyns: ΔNterm, ΔNAC, and ΔCterm. SPR analysis demonstrated ΔNAC and ΔCterm but not ΔNterm segments showing binding affinity for G4tr, suggesting that the N-terminus of αSyn preferentially binds to rG4s (**Extended Data Fig. 4c, d**). We also obtained similar results using the Quartz Crystal Microbalance system.

As for αSyn LLPS *in vitro*, G4mt demonstrated no additional effects on αSyn droplet formation in the presence of 15% PEG, while G4tr evoked αSyn transition into gel-like states (**Fig. 1i**). Furthermore, αSyn ΔNterm mutant formed droplets but not gel-like aggregates with G4tr (**Extended Data Fig. 4e**). In FRAP studies, the fluorescence recovery of αSyn droplets was rapid when formed alone, with G4mt, and as ΔNterm with G4tr, whereas that of gel-like assemblies with G4tr was not recovered (**Fig. 1i** and **Extended Data Fig. 4e**). The intensity of Proteostat signals was significantly higher in gel-like assemblies of αSyn with G4tr compared to that in droplets of αSyn alone, αSyn with G4mt, and ΔNterm with G4tr (**Fig. 1j** and **Extended Data Fig. 4f**). Considered together, rG4s bind directly to the N-terminus of αSyn, accelerating the sol–gel phase transition *in vitro*.

Ca^{2+}-induced rG4 assembly is essential for αSyn aggregation

We examined the intracellular mechanism underlying the rG4s-induced αSyn aggregation on pathological conditions. rG4 itself has the propensity to undergo LLPS *in vitro*, which can be boosted electrostatically by Mg^{2+} divalent cation[16,18]. Indeed, G4tr underwent LLPS without PEG; however, G4mt did not (**Extended Data Fig. 5a**). Moreover, other divalent cation Ca^{2+} promoted G4tr LLPS droplets and enlarged the size of droplets (**Extended Data Fig. 5a,b**). Furthermore, the Ca^{2+}-induced increase in droplet size was markedly suppressed by the addition of EGTA, a Ca^{2+} chelator (**Extended Data Fig. 5b**). Notably, G4tr droplets co-aggregated with αSyn in the presence of Ca^{2+} (**Fig. 2a**). In the absence of G4tr, αSyn droplets or gel-like aggregates were not observed regardless of the presence of Ca^{2+} (**Fig. 2a**). Ca^{2+} transitioned G4tr-αSyn coacervates to a gel-like state thereby significantly reducing FRAP, whose effect was abolished by EGTA (**Fig. 2b**). As expected, Proteostat signals were detected only in the G4tr-αSyn complex in the presence of Ca^{2+} (**Fig. 2c**). Moreover, lower concentration of αSyn (34.5 μM) underwent sol–gel transition in the presence of G4tr and Ca^{2+} (**Extended Data Fig. 5c**).

These results suggested that Ca^{2+}-induced rG4 assembly is essential for the efficient initiation of αSyn aggregation.

The persistent and excessive Ca^{2+} entry in neurons by certain metabolic stress conditions could be a major factor in the development of neurodegeneration, including PD[32,33]. Indeed, in response to PFF-induced cellular stress, cultured neurons demonstrated an excessively elevated intracellular Ca^{2+} concentration (**Extended Data Fig. 5d**)[34]. Thus, we examined whether Ca^{2+}-induced rG4 assembly is observed in neurons by immunostaining with G4-specific antibody BG4[35]. PFF and Ca^{2+} ionophore (ionomycin) treatments significantly increased the number of cytosolic G4 granules of both small (0.05–0.2 μm^2) and large (> 0.2 μm^2) sizes compared to vehicle-treated controls (**Fig. 2d**). Furthermore, the number of G4 granules co-localized with αSyn significantly increased after PFF treatment (**Extended Data Fig. 6a**). Eight days after PFF treatment, pS129-positive aggregates were extensively co-localized with G4 granules in mouse cultured neurons (**Fig. 2e**). In the synucleinopathy model mice injected with PFF into the dorsal striatum, pS129-positive inclusions were observed in the tyrosine hydroxylase (TH)-positive dopaminergic (DA) neurons of the substantia nigra, which co-localized with large G4 granules (**Fig. 2f**). In the brainstems of postmortem human patients with PD, the majority (> 90%) of pS129-positive inclusions co-localized with large G4 granules (**Fig. 2g** and **Extended Data Fig. 6b**). The immunoreactivity of cytosolic G4 granules seen in asymptomatic controls was completely eliminated by RNase pretreatment, whereas immunoreactivity of cytosolic G4 granules co-localized with pS129-positive inclusions in PD brains was not (**Extended Data Fig. 6b**).

αSyn co-accumulated with rG4 containing synaptic mRNAs following Ca^{2+} overload

To identify the rG4s as scaffolds of αSyn aggregation in neurons, BG4-bound RNAs were analyzed in PFF-treated cultured mouse neurons using RNA immunoprecipitation coupled with sequencing (BG4 RIP-seq)[18].

We identified 254 and 524 gene transcripts enriched in vehicle- and PFF-treated neurons, respectively, of which 162 were common (cutoff: P-value < 0.05 and fold-change > 1.5) (**Fig. 3a** and **Supplementary Tables 2 and 3**). We compared fragments per kilobase of exon per million mapped reads (FPKM) obtained from BG4-enriched fractions with those from IgG-treated fractions to identify the rG4s. To predict quadruplex-forming guanine-rich sequences (QGRS) mapper[36], more than 95% of BG4-enriched mRNAs were found to have putative rG4-forming sequences with two or three G-tetrad layers (**Fig. 3b, Extended Data Fig. 7a** and **Supplementary Table 4,5**). In the gene ontology (GO) analysis, BG4-binding RNAs obtained from PFF-treated neurons

236 contributed to neurodegeneration (**Extended Data Fig. 7b** and **Supplementary Tables 6**
237 **and 7**), and most of these RNAs were linked to the synapse (**Fig. 3c** and **Supplementary**
238 **Table 8**). Among the rG4 enriched in PFF-treated neurons, we focused on two mRNAs
239 encoding synaptic proteins, *Camk2a* and *dlg4*, which have been validated to fold into G4
240 structures by biophysical assays[37] and conserved in both mice and humans (**Extended**
241 **Data Fig. 7c**). Moreover, these synaptic proteins (i.e., CaMKIIα and PSD95) are essential
242 for synaptic plasticity, an important cellular mechanism underlying learning and
243 memory[38,39]. We also validated that both mRNAs contain rG4-forming sequences (G4ck
244 and G4ps; **Fig. 3d** and **Extended Data Fig. 7d**). Both G4ck and G4ps co-aggregated with
245 αSyn in the presence of Ca^{2+} *in vitro*, which were detected by Proteostat (**Fig. 3e** and
246 **Extended Data Fig. 7e**). To obtain an insight into the interaction of αSyn with these
247 mRNAs in the context of pathogenesis, we performed *in situ* hybridization together with
248 immunostaining in mouse cultured cortical neurons eight days after PFF treatment. We
249 observed high co-localization of these mRNAs with pS129-positive aggregates in the
250 cytoplasm (**Fig. 3f** and **Extended Data Fig. 7f**).
251
252 **Optogenetics-induced rG4 assembly evokes αSyn aggregation and neuronal**
253 **dysfunction**
254 To provide direct evidence that rG4 assembly induces αSyn aggregation, we
255 developed an optogenetics-induced rG4 assembly approach, "optoG4 system" under
256 spatiotemporal control of blue light (BL) stimulation. The optoG4 system consists of two
257 plasmids: *G4tr-MS2* RNA—rG4-forming $(TTAGGG)_{23}$ repeats tagged 12×*MS2*-hairpin
258 loops[40] and MCP-Cry2—*MS2*-coat protein tagged mCh-Cry2olig, which functions by co-
259 expressing them in the cells (**Fig. 4a** and **Extended Data Fig. 8a**). We confirmed that
260 MCP-Cry2 clusters were formed in the optoG4-expressing Neuro-2a cells in a BL
261 exposed-time dependent manner (**Fig. 4b**). In the cells co-expressing optoG4 and αSyn,
262 MCP-Cry2 clusters co-assembled with αSyn and *G4tr-MS2* RNA 3-h following BL
263 stimulation (**Fig. 4c**). The BL-induced αSyn granules were p62-, pS129-, and BG4-
264 positive (**Extended Data Fig. 8b, c**). Since Cry2olig possesses the property of reversible
265 homo-oligomerization in response to BL stimulation[41], we examined whether BL-induced
266 αSyn aggregation in the optoG4 system is irreversible. In the cells co-expressing optoG4
267 and αSyn, MCP-Cry2 formed irreversible complexes containing αSyn and *G4tr-MS2*
268 RNA following 3-h BL stimulation and subsequent 3-h withdrawal (**Extended Data Fig.**
269 **8d, e**). However, MCP-Cry2 clusters were significantly more dispersed in cells expressing
270 only optoG4 than in cells co-expressing optoG4 and αSyn under the same stimulatory
271 condition (**Extended Data Fig. 8d, e**). We developed "optoG4mt system" using *G4mt-*

MS2 RNA consisting of rG4-unforming $(TTACCG)_{23}$ repeats tagged 12×*MS2*-hairpin loops as a negative control for rG4-forming structure (**Extended Data Fig. 8a, b**). In cells co-expressing optoG4mt and αSyn, MCP-Cry2 and *G4mt-MS2* RNA complexes formed 3-h after BL stimulation; however, they did not co-assemble with αSyn or G4s (**Extended Data Fig. 8f**).

In mouse cultured cortical neurons expressing the optoG4 system, endogenous αSyn formed pS129- and p62-positive aggregates following 3-h BL stimulation (**Fig. 4d** and **Extended Data Fig. 8g**), but did not in those expressing optoG4mt (**Fig. 4e**) or MCP-Cry2 alone (**Extended Data Fig. 8h**). Endogenous αSyn aggregation induced by optoG4 were retained even after 3-h BL stimulation and subsequent 3-h withdrawal (**Extended Data Fig. 8i**). We measured spontaneous excitatory postsynaptic currents (sEPSCs) to investigate the effect of optoG4-induced αSyn aggregation on neuronal activity. The sEPSC amplitude and frequency were significantly reduced in BL-stimulated optoG4 neurons compared to non-stimulated optoG4 neurons (**Fig. 4f**). Changes in the neuronal activities were not observed in the neurons expressing MCP-Cry2 alone or with optoG4mt, regardless of the BL conditions (**Fig. 4f** and **Extended Data Fig. 8j**). Impaired sEPSCs in the BL-stimulated optoG4 neurons were also sustained after 3-h BL withdrawal (**Extended Data Fig. 8k**).

Thereafter, we employed the optoG4 system in a series of *in vivo* experiments, injecting recombinant adeno-associated viruses (AAVs) into the nigral DA neurons of mice resulting in expression of improved Cre under the control of mouse TH promoter (AAV-mTH-iCre[42]), iCre recombinase-dependent expression of MCP-Cry2 flanked by double-floxed inverse open reading frame (DIO) (AAV- MCP-Cry2), and *G4tr-MS2* RNA (AAV-*G4-MS2*). Fourteen days after AAV injection, mice were implanted with a wireless optogenetic device to enable BL stimulation in the substantia nigra. Two days after the implantation, the mice were subjected to BL stimulation for 1-h per day for four weeks (**Fig. 4g**).

Immunohistochemical analysis confirmed MCP-Cry2 expression in the nigral DA neurons (**Extended Data Fig. 9a**). In optoG4 mice, BL stimulation formed αSyn granules, which co-assembled with MCP-Cry2 and *G4-MS2* RNA (**Fig. 4h**). In optoG4 mice with BL, the number of TH-positive DA neurons was significantly reduced compared to that without BL, and pS129-positive inclusions were observed (**Fig. 4i**). No pathological changes were observed in the other groups (**Extended Data Fig. 9b, c**). Rotarod and beam-walking tests were performed to determine whether optoG4 system induces PD-like motor deficits. OptoG4 mice with BL demonstrated a progressive and significant decrease in fall latency in the rotarod test and increase in the number of footslips in the

308 beam-walking test compared to those without BL (**Fig. 4j**). The other groups did not show
309 motor deficits, regardless of BL stimulation (**Extended Data Fig. 9d**).
310
311 **Treatment with 5-ALA ameliorates motor dysfunctions observed in PFF-injected**
312 **mice**
313 Since PPIX binds to rG4s[9], we examined whether PPIX affects rG4s assembly *in*
314 *vitro*. Treatment with PPIX reduced the size of G4tr-containing liquid droplets (**Fig. 5a**).
315 Importantly, the formation of gel-like aggregates consisting of G4tr and αSyn was also
316 inhibited by PPIX (**Fig. 5b** and **Extended Data Fig. 10a**).
317 PPIX is not available *in vivo* owing to its cytotoxicity[43]; thus, we investigated
318 whether 5-ALA, an extremely low-toxic and blood–brain barrier-permeable prodrug of
319 PPIX[9,29], could inhibit αSyn aggregation in cells. The application of 5-ALA significantly
320 prevented increase in G4 granules and αSyn aggregation 24-h following PFF treatment in
321 Neuro-2a cells expressing mCh-αSyn (**Fig. 5c** and **Extended Data Fig. 10b**). Thereafter,
322 5-ALA was administered to primary mouse cultured PFF-treated neurons. 5-ALA
323 significantly restored the reduction in amplitude and frequency in sEPSC eight days after
324 co-treatment with PFF (**Fig. 5d**). 5-ALA also reduced the pS129-positive inclusions (**Fig.**
325 **5e**), and attenuated reduction of PSD95 and CaMKIIα protein levels without changes in
326 the mRNA levels of *Dlg4* and *Camk2a* in PFF-treated neurons (**Fig. 5f and Extended**
327 **Data Fig. 10c**).
328 Finally, we investigated the effects of 5-ALA on αSyn aggregation and
329 Parkinsonism *in vivo*. Mice were injected with PFF into the dorsal striatum followed by
330 daily oral administration of 5-ALA (1 or 3 mg/kg/day). Two months after PFF injection,
331 5-ALA (3 mg/kg) prevented motor dysfunctions in PFF-injected mice (**Fig. 5g**).
332 Importantly, 5-ALA also prevented the formation of pS129-positive inclusion and the
333 resultant degeneration of nigral DA neurons (**Fig. 5h**).
334
335

336 **Discussion**

337 In this study, we demonstrated that Ca^{2+}-induced rG4 assembly via LLPS served
338 as scaffolds for αSyn aggregation, contributing to neurodegeneration. rG4s bind directly
339 to the N-terminus of αSyn, accelerating the aggregation. In PFF-treated neurons, αSyn
340 aggregated with rG4 assembly composed of synaptic mRNAs, such as *Camk2a* and *Dlg4,*
341 due to Ca^{2+} excess influx, eliciting neuronal dysfunction. In addition, rG4 assembly by
342 the optoG4 system caused endogenous αSyn aggregation and neuronal dysfunction,
343 reproducing the pathology of synucleinopathies. 5-ALA and PPIX administration
344 suppressed rG4 LLPS and inhibited the co-aggregation of rG4s and αSyn, thereby
345 ameliorating neurodegeneration and motor deficits in PFF-injected synucleinopathy mice.
346 Considered together, rG4 assembly attributed to aberrant intracellular Ca^{2+} influx
347 promotes αSyn aggregation, which may be involved in the pathogenesis of
348 synucleinopathies **(Extended data Fig. 10**).

349 Although the aggregation of many neurodegenerative disease-related IDPs has
350 been attributed to LLPS-mediated sol–gel phase transitions[22,23,24,25,44], purified αSyn does
351 not form liquid droplets nor aggregates *in vitro*, except under non-physiological
352 conditions, such as high protein concentrations above 100 μM, addition of molecular
353 crowding reagents, low pH, and agitation (**Fig. 1**)[21,45,46,47]. The difficulty of αSyn
354 aggregation *in vitro* is presumably attributed to the monomeric state preserved by biased
355 electrostatic and hydrophobic intramolecular interactions and intermolecular repulsion.
356 αSyn has opposite charges at the N- and C-termini and has overall low hydrophobicity;
357 the N-terminus with positively charged, the NAC region with high hydrophobicity, and
358 the C-terminus with highly negatively charged that binds to bivalent metal ions, including
359 Ca^{2+}[48,49]. The long-range electrostatic interactions through the N- and C-termini, as well
360 as hydrophobic interactions between the C-terminus and NAC regions form a compact,
361 autoinhibitory conformation that limits the exposure of the NAC region. In addition,
362 intermolecular interactions of the negatively charged C-terminus produce electrostatic
363 repulsion, inhibiting multimer formation[48,49].

364 Distinct from "αSyn LLPS", we here proposed the "rG4 LLPS" hypothesis that
365 Ca^{2+}-induced association of rG4s via LLPS is responsible for the initiation of αSyn
366 aggregation. The rG4-induced αSyn aggregation occurred under near physiological
367 conditions (neutral pH, concentration at 34.5 μM) without both agitation and the presence
368 of the molecular crowding reagent (**Extended Data Fig. 5**). The preferential binding of
369 the N-terminus of αSyn to rG4s was required for αSyn aggregation **(Extended Data Fig.
370 4e, f**). Since the N-terminus of αSyn is involved in membrane anchoring[31], a critical
371 period could exist at which the interaction factor with αSyn shifts from the membrane to

372 rG4s in the pathogenic process. Importantly, both rG4s and Ca^{2+} are necessary and
373 sufficient for αSyn aggregation. Since rG4 unfolding mutant G4mt did not bind to αSyn,
374 the binding of rG4s to αSyn was not through the electrostatic interaction of the negatively
375 charged phosphate backbone of the RNAs with the positively charged N-terminus of the
376 protein. Although how rG4 modulates αSyn conformation and the subsequent aggregation
377 is unclear, it is possible that rG4s and Ca^{2+} shield both the N-terminus and negatively
378 charged C-terminus, respectively, thereby exposing the NAC region upon release of the
379 compact conformation. This would result in αSyn bearing aggregation-prone states via
380 the hydrophobic core domain (NAC-NAC interaction). More structural analyses are
381 warranted in the rG4s binding to the N-terminus through non-covalent bonds, such as
382 hydrogen bonds and hydrophobic interactions using cryogenic electron microscopy and
383 X-ray crystallography techniques.

384 In mammals, rG4-forming potential sequences are abundant in transcripts, with
385 3,800 predicted in approximately 2,300 different genes[50]. Although the rG4 assembly
386 organizes the formation of SGs in neurons[18], the intracellular mechanism of the rG4
387 assembly attributed to stress stimulation remains unclear. We here proposed that persistent
388 and excessive intracellular Ca^{2+} influx by PFF treatment triggers rG4 assembly (**Fig. 2**).
389 Interestingly, mRNAs encoding synaptic proteins accounted for most of the RNAs
390 identified by BG4 RIP-seq in the PFF-treated neurons (**Fig. 3**). Consistent with this result,
391 a significant reduction in the synaptic activity was observed in neurons challenged with
392 optoG4 system and PFF (**Figs. 4 and 5**). Indeed, excessive Ca^{2+} influx has been identified
393 in the pathogenesis of various neurodegenerative diseases, including synucleinopathies,
394 Alzheimer's disease, amyotrophic lateral sclerosis, Huntington's disease, and
395 spinocerebellar ataxias[32]. Furthermore, rG4-induced sol–gel phase transition of tau has
396 been observed *in vitro* (under preparation). These results suggest that rG4 is a key factor
397 in the aggregation of prionoid proteins, including αSyn, tau, and FMRpolyG[9], and
398 excessive Ca^{2+} influx-induced rG4 assembly may be a main source of the pathogenesis in
399 neurodegenerative diseases. In the future, it is necessary to elucidate why neuronal rG4
400 assembly contains a majority of synaptic mRNAs and how rG4 assembly aggregation of
401 prionoid proteins contributes to the pathogenesis of neurodegeneration.

402 In conclusion, rG4 assembly by excessive Ca^{2+} influx could induce αSyn
403 aggregation and neuronal dysfunction. In addition, we found that PPIX can inhibit the
404 rG4 assembly, and its prodrug 5-ALA significantly ameliorated motor deficits in PFF-
405 injected mice. Importantly, 5-ALA can act on the brain through oral administration and
406 produce PPIX intracellularly without serious adverse effects[29]. 5-ALA can be
407 prophylactically administered before progressive motor dysfunction, and could be a

408 promising novel agent for neurodegenerative diseases, including synucleinopathies.
409

410 **Main references**

411

412 1. Spillantini, M.G. et al. Alpha-synuclein in Lewy bodies. *Nature* **388**, 839–840 (1997).

413

414 2. Spillantini, M.G., Crowther, R.A., Jakes, R., Hasegawa, M. & Goedert, M. α-
415 Synuclein in filamentous inclusions of Lewy bodies from Parkinson's disease and
416 dementia with Lewy bodies. *Proc. Natl. Acad. Sci. U.S.A.* **95**, 6469–6473 (1998).

417

418 3. Spillantini, M.G. & Goedert, M. The alpha-synucleinopathies: Parkinson's disease,
419 dementia with Lewy bodies, and multiple system atrophy. *Ann. N. Y. Acad. Sci.* **920**,
420 16–27 (2000).

421

422 4. Conway, K.A., Harper, J.D. & Lansbury P.T. Accelerated in vitro fibril formation by
423 a mutant alpha-synuclein linked to early-onset Parkinson disease. *Nat. Med.* **4**, 1318–
424 1320 (1998).

425

426 5. Conway, K.A. et al. Acceleration of oligomerization, not fibrillization, is a shared
427 property of both alpha-synuclein mutations linked to early-onset Parkinson's disease:
428 implications for pathogenesis and therapy. *Proc. Natl. Acad. Sci. U.S.A.***97**, 571–576
429 (2000).

430

431 6. Serpell, L.C., Berriman, J., Jakes, R., Goedert, M. & Crowther, R.A. Fiber diffraction
432 of synthetic α-synuclein filaments shows amyloid-like cross-β conformation. *Proc.*
433 *Natl. Acad. Sci. U.S.A.* **97**, 4897–4902 (2000).

434

435 7. Stefanis, L. α-Synuclein in Parkinson's disease. *Cold Spring Harb. Perspect. Med.* **2**,
436 a009399 (2012).

437

438 8. Oliveira, L.M.A. et al. Alpha-synuclein research: defining strategic moves in the
439 battle against Parkinson's disease. *N.P.J. Parkinsons Dis*. **7**, 65 (2021).

440

441 9. Asamitsu, S. et al. CGG repeat RNA G-quadruplexes interact with FMRpolyG to
442 cause neuronal dysfunction in fragile X-related tremor/ataxia syndrome. *Sci. Adv.* **7**,
443 eabd9440 (2021).

444

445 10. Maroteaux, L., Campanelli, J.T. & Scheller, R.H. Synuclein: a neuron-specific

446 protein localized to the nucleus and presynaptic nerve terminal. *J. Neurosci.* **8**, 2804–
447 2815 (1988).
448
449 11. Theillet, F.X. et al. Structural disorder of monomeric alpha-synuclein persists in
450 mammalian cells. *Nature* **530**, 45–50 (2016)
451
452 12. Snead, D. & Eliezer, D. Intrinsically disordered proteins in synaptic vesicle
453 trafficking and release. *J. Biol. Chem.* **294**, 3325–3342 (2019).
454
455 13. Brangwynne, C.P. et al. Germline P granules are liquid droplets that localize by
456 controlled dissolution/condensation. *Science* **324**, 1729–1732 (2009).
457
458 14. Kato, M. et al. Cell-free formation of RNA granules: low complexity sequence
459 domains form dynamic fibers within hydrogels. *Cell* **149**, 753–767 (2012).
460
461 15. Hyman, A.A., Weber, C.A., & Julicher, F. Liquid-liquid phase separation in biology.
462 *Annu. Rev. Cell Dev. Biol.* **30**, 39–58 (2014).
463
464 16. Jain, A., Vale, R.D. RNA phase transitions in repeat expansion disorders. *Nature*. **546**,
465 243–247 (2017).
466
467 17. Alberti, S., Gladfelter, A. & Mittag, T. Considerations and Challenges in Studying
468 Liquid-Liquid Phase Separation and Biomolecular Condensates. *Cell* **176**, 419–434
469 (2019).
470
471 18. Asamitsu, S. et al. RNA G-quadruplex organizes stress granule assembly through
472 DNAPTP6 in neurons. *Sci. Adv.* **9**, eade2035 (2023).
473
474 19. Shin, Y. & Brangwynne, C.P. Liquid phase condensation in cell physiology and
475 disease. *Science.* **357**, eaaf4382 (2017).
476
477 20. Wolozin, B. & Ivanov, P. Stress granules and neurodegeneration. *Nat. Rev. Neurosci.*
478 **20**, 649–666 (2019).
479
480 21. Ray, S. et al. Datta α-Synuclein aggregation nucleates through liquid-liquid phase
481 separation *Nat. Chem.* **12**,705–716 (2020).

22. Wegmann, S. et al. Tau protein liquid–liquid phase separation can initiate tau aggregation. *E.M.B.O. J.,***37**, e98049 (2018).

23. Patel, H.O. et al. A Liquid-to-Solid Phase Transition of the ALS Protein FUS Accelerated by Disease Mutation *Cell* **162**, 1066-1077 (2015).

24. Conicella, A.E., Zerze, G.H., Mittal, J. & Fawzi, N.L. ALS Mutations Disrupt Phase Separation Mediated by α-Helical Structure in the TDP-43 Low-Complexity C-Terminal Domain. *Structure* **24**, 1537–1549 (2016).

25. Molliex, J. et al. Phase separation by low complexity domains promotes stress granule assembly and drives pathological fibrillization.**163**, 123–133 (2015).

26. Kim, J., Cheong, C. & Moore P.B. Tetramerization of an RNA oligonucleotide containing a GGGG sequence. *Nature* **351**, 331–332 (1991).

27. Laura, A. et al. Exogenous α-synuclein fibrils induce Lewy body pathology leading to synaptic dysfunction and neuron death. *Neuron* **72**, 57–71 (2011).

28. Luk, K.C. et al. Pathological α-synuclein transmission initiates Parkinson-like neurodegeneration in nontransgenic mice. *Science* **338**, 949–953 (2012).

29. Shioda, N. et al. Targeting G-quadruplex DNA as cognitive function therapy for ATR-X syndrome. *Nat. Med.* **24**, 802–813 (2018).

30. Lambert, N. et al. RNA Bind-n-Seq: quantitative assessment of the sequence and structural binding specificity of RNA binding proteins. *Mol. Cell.* **54**, 887–900 (2014).

31. Goedert, M. Alpha-synuclein and neurodegenerative diseases. *Nat. Rev. Neurosci.* **2**, 492–501 (2001).

32. Bezprozvanny, I. Calcium signaling and neurodegenerative diseases. *Trends Mol Med.* **15**, 89–100 (2009).

33. Surmeier, D.J., Guzman, J.N., Sanchez-Padilla, J. Calcium, cellular aging, and

518 selective neuronal vulnerability in Parkinson's disease. *Cell Calcium.* **47,** 175–182
519 (2010).
520
521 34. Danzer, K. M., et al. Different species of alpha-synuclein oligomers induce calcium
522 influx and seeding. *J. Neurosci.* **27**, 9220–9232 (2007).
523
524 35. Biffi, G., Di Antonio, M., Tannahill, D. & Balasubramanian, S. Visualization and
525 selective chemical targeting of RNA G-quadruplex structures in the cytoplasm of
526 human cells. *Nat. Chem.* **6**, 75–80 (2014).
527
528 36. Kikin, O., D'Antonio, L. & Bagga, P.S. QGRS Mapper: a web-based server for
529 predicting G-quadruplexes in nucleotide sequences. *Nucleic Acids Res.* **34**, W676–
530 W682 (20006.
531
532 37. Subramanian, M., et al. G-quadruplex RNA structure as a signal for neurite mRNA
533 targeting. *E.M.B.O. Rep*. **12**, 697–704 (2011).
534
535 38. Silva, A.J., Stevens, C.F., Tonegawa, S. & Wang, Y. Deficient hippocampal long-term
536 potentiation in alpha-calcium-calmodulin kinase II mutant mice. *Science.* **257**, 201–
537 206 (1992).
538
539 39. Migaud, M. et al. Enhanced long-term potentiation and impaired learning in mice
540 with mutant postsynaptic density-95 protein. *Nature* **396**, 433–439 (1998).
541
542 40. Bertrand E, et al. Localization of ASH1 mRNA particles in living yeast. *Molecular*
543 *Cell.* **2**, 437–445 (1998).
544
545 41. Taslimi, J.D. et al. Tucker An optimized optogenetic clustering tool for probing
546 protein interaction and function *Nat. Commun.* **5**, 4925 (2014).
547
548 42. Chan, K.Y. et al. Engineered AAVs for efficient noninvasive gene delivery to the
549 central and peripheral nervous systems. *Nat. Neurosci.* **20**, 1172–1179 (2017).
550
551 43. Sachar, M., Anderson, K.E. & Ma, X. Protoporphyrin IX: the Good, the Bad, and the
552 Ugly. *J. Pharmacol. Exp. Ther.* **356**, 267–75 (2016).
553

44. Zbinden, A., Pérez-Berlanga, ., P., De Rossi, P. & Polymenidou M. Phase Separation and Neurodegenerative Diseases: A Disturbance in the Force. Dev. *Cell* **55**, 45–68 (2020).

45. Kumar, R. et al. Cytotoxic Oligomers and Fibrils Trapped in a Gel-like State of α-Synuclein Assemblies. *Angew. Chem. Int. Ed. Engl*. **57**, 5262–5266 (2018).

46. Hardenberg, M.C. et al. Observation of an α-synuclein liquid droplet state and its maturation into Lewy body-like assemblies. *J. Mol. Cell Biol.* **13**, 282–294 (2021).

47. Sawner, A.S. et al. Modulating α-Synuclein Liquid-Liquid Phase Separation. *Biochemistry* **60**, 3676–3696 (2021).

48. Stephens, A.D., Zacharopoulou, M. & Kaminski Schierle, GS. The Cellular Environment Affects Monomeric α-Synuclein Structure. *Trends Biochem. Sci.* **44**, 453–466 (2019).

49. Stephens, A.D. et al. Extent of N-terminus exposure of monomeric alpha-synuclein determines its aggregation propensity. *Nat. Commun.* **11**, 2820 (2020).

50. Kwok, C.K., Marsico, G., Sahakyan, A.B., Chambers, V.S. & Balasubramanian, S. rG4-seq reveals widespread formation of G-quadruplex structures in the human transcriptome. *Nat. Methods.* **13**, 841–844 (2016).

Figures and Figure legends

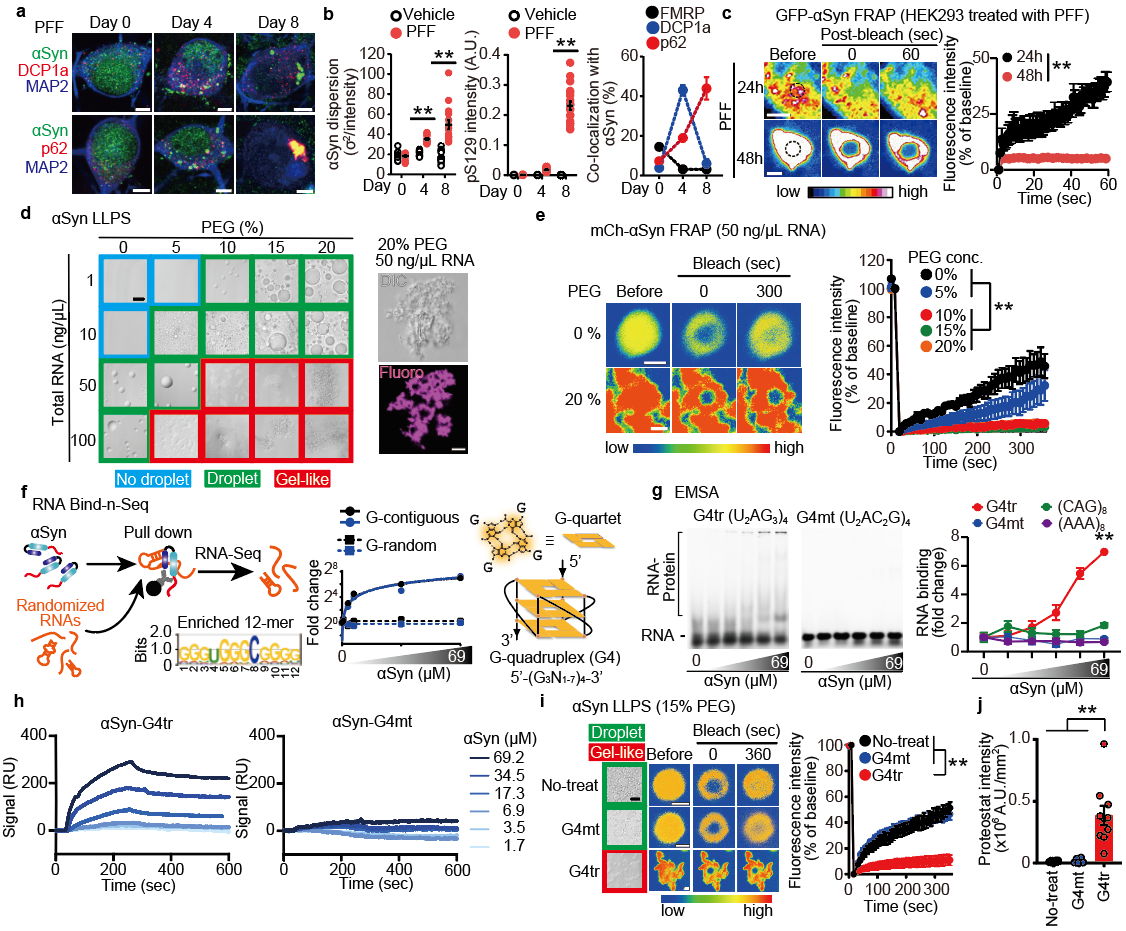

Fig. 1: RNA G-quadruplexes initiate α-synuclein (αSyn) sol–gel phase transition. **a**, Representative images of MAP2 (blue) and mouse αSyn (green) with DCP1a or p62 (red) in mouse cultured neurons following pre-formed fibril (PFF) treatment. Scale bars, 5 μm. **b**, Analyses of αSyn dispersion (left), pS129^{+} immunoreactivity relative to MAP2^{+} area (center), and co-localization of αSyn with markers of RNA granule and aggresome (right) in mouse cultured neurons after PFF treatment (images shown in **Extended Data Fig. 1b, c**). **c**, αSyn fluorescence recovery after photobleaching (FRAP) assay of PFF-treated HEK293T cells following transient expression of GFP-αSyn. Scale bars, 2 μm. **d**,**e**, *In vitro* αSyn phase separation (d) and FRAP assay (e) dependent on polyethylene glycol (PEG) and total RNA. Scale bars, 5 and 1 μm, respectively. DIC, differential interference contrast. **f**, Schematic of RNA Bind-n-Seq experiment for αSyn and the top enriched RNA motif (left). Fold enrichment of the top two 12-mers (circle marks) and two randomly chosen 12-mers (square marks) across αSyn concentrations (0, 0.69, 3.45, 6.9, 34.5, and 69 μM; center). Schematic illustration of intramolecular parallel G4 (right). **g**, electrophoresis mobility shift assay for the interaction of αSyn with RNA oligomers in the presence of 100 mM NaCl. αSyn concentrations were the same as those of RNA Bind-

n-Seq (**f**). **h**, surface plasmon resonance sensorgrams for the interaction of αSyn with G4tr or G4mt. RU, response unit. **i**, *In vitro* αSyn phase separation (left) and FRAP assay (right) with G4tr or G4mt in the presence of 15% PEG. Scale bars, 5 and 1 μm, respectively. **j**, Proteostat intensity within phase-separated RNA/αSyn in the presence of 15% PEG. Data are presented as mean ± standard error of mean. $^{**}P < 0.01$ by two-way (**b**,**c**,**e**,**g** and **i**) and one-way (**j**) Analysis of variance with Bonferroni's multiple comparisons test. Number of replicates is shown in Supplementary Table 9.

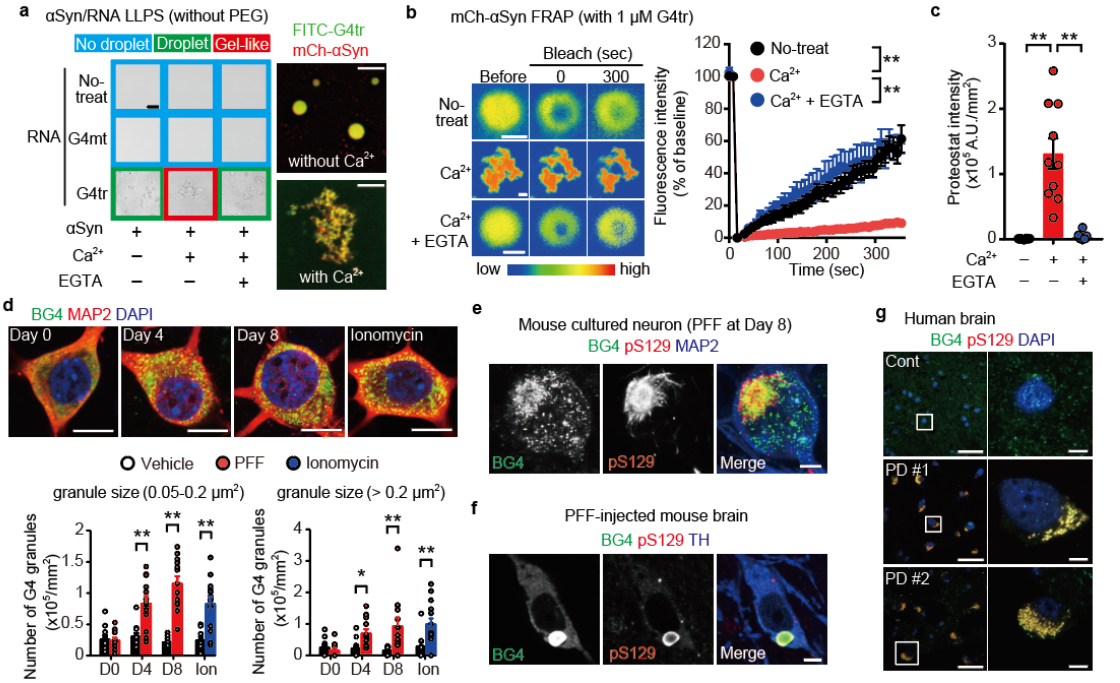

Fig. 2: Ca^{2+} triggers RNA G-quadruplexes -induced α-synuclein (αSyn) sol–gel phase transition.

a, Representative images of *in vitro* αSyn phase transition dependent on G4tr and Ca^{2+}. Scale bars, 10 (left) and 5 (right) μm, respectively. Veh., vehicle. **b**, *In vitro* αSyn fluorescence recovery after photobleaching assay dependent on G4tr and Ca^{2+}. Scale bars, 1 μm. **c**, Proteostat intensity within phase-transitioned RNA/αSyn dependent on Ca^{2+}. **d**, Representative images (top) and quantification of the number (bottom) of BG4 granules (green) in primary cultured mouse neurons treated with pre-formed fibrils (PFF) or Ionomycin (Ion; 30 min). Scale bars, 10 μm. **e–g**, Representative images of BG4 (green) and pS129 (red) with MAP2, TH, or 4',6-diamidino-2-phenylindole (blue) in PFF-treated mouse cultured neurons (**e**), PFF-injected mouse brain (**f**), and human normal control and postmortem brains of patients with Parkinson's disease (**g**). Low and high magnification scale bars, 20 and 5 μm, respectively. Data are presented as mean ± standard error of mean. $^{**}P < 0.01$ by two-way (**b**,**d** (vehicle vs. PFF)) and one-way (**c**) Analysis of variance with Bonferroni's multiple comparisons test and by two-sided, unpaired Student's *t*-test (**d** (vehicle vs. Ionomycin)). Number of replicates is shown in Supplementary Table 9.

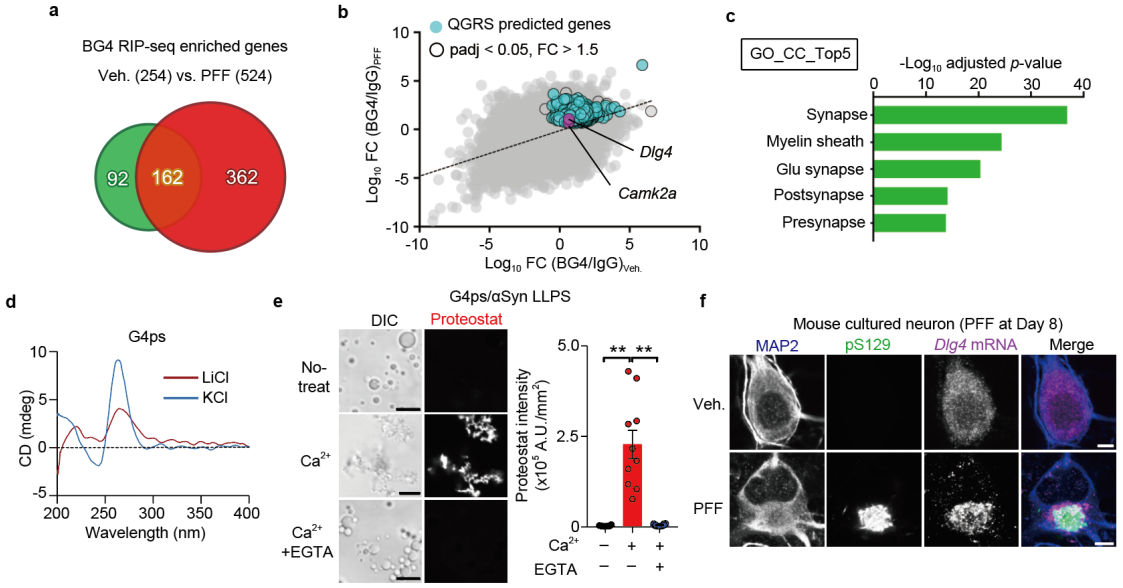

Fig. 3: RNA G-quadruplexes-containing synaptic mRNA are involved in α-synuclein (αSyn) aggregation.

a, Venn diagram of BG4-enriched RNAs in vehicle- and pre-formed fibrils (PFF)-treated mouse cultured neurons compared with immunoglobulin G (IgG) control. **b**, Scatter plots of BG4-enriched RNAs in vehicle versus PFF treatment. Open black dots show RNAs with $P < 0.05$ and fold-change (FC) > 1.5, and light blue dots exhibit predicted genes in the quadruplex-forming guanine-rich sequences (QGRS) mapper. **c**, Gene Ontology (GO) enrichment analysis by cellular component (CC) terms in BG4-enriched RNAs only detected in PFF-treated mouse cultured neurons. **d**, Circular dichroism (CD) spectra of mouse G4ps (sequence shown in **Extended Data Fig. 9c**) in the presence of KCl or LiCl. **e**, Representative images (left) and quantification (right) of Proteostat intensity within phase-transitioned G4ps/αSyn dependent on Ca^{2+}. Scale bars, 5 μm. **f**, Representative confocal images of MAP2 (blue), pS129 (green), and *Dlg4* RNA (magenta) in mouse cultured neurons following PFF treatment. Scale bars, 5 μm. Data are presented as mean ± standard error of mean. $^{**}P < 0.01$ by one-way analysis of variance with Bonferroni's multiple comparisons test. Number of replicates is shown in Supplementary Table 9.

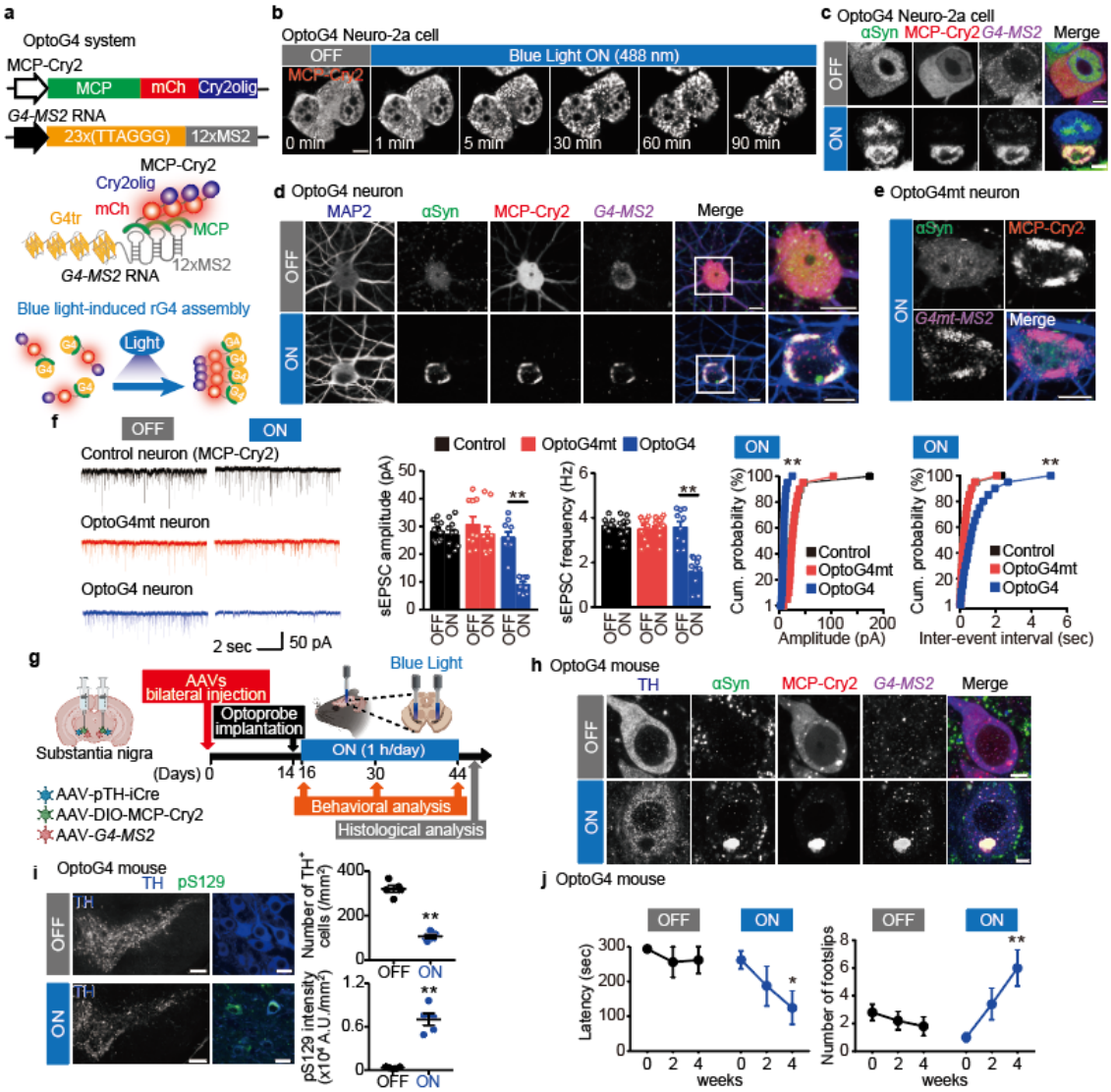

Fig. 4: OptoG4-induced α-synuclein (αSyn) aggregation triggers neurodegeneration. **a**, Schematic of the light-inducible RNA G-quadruplexes assembly approach using the Cry2olig photoreceptor, MCP protein, and 12×*MS2*-hairpin loops. **b**, Representative time-lapse images of Neuro-2a cells challenged with blue light (BL) for the indicated time under expression of optoG4. Scale bar, 20 μm. **c**, Representative images of αSyn (green), MCP-Cry2 (red), *G4-MS2* RNA (magenta), and 4',6-diamidino-2-phenylindole (blue) in optoG4 and αSyn co-expressing Neuro-2a cells with or without exposure to BL stimulation. Scale bars, 5 μm. **d**,**e**, Representative images of MAP2 (blue), αSyn (green), MCP-Cry2 (red), and *MS2* RNA fluorescent *in situ* hybridization (magenta) in optoG4 (**d**) and optoG4mt (**e**) mouse cultured neurons exposed to BL stimulation or darkness. Scale bars, 10 μm. **f**, Measurement of spontaneous excitatory postsynaptic currents (sEPSCs) in MCP-Cry2 (control)-, optoG4mt-, and optoG4-expressing mouse cultured neurons with BL stimulation. Cum., Cumulative. **g**, Schematic of viral constructs for *in*

651 *vivo* optoG4 modeling and experimental schedules. **h**, Representative images of tyrosine
652 hydroxylase (TH) (blue), αSyn (green), MCP-Cry2 (red), and *G4-MS2* RNA (magenta)
653 in the nigral dopaminergic neurons exposed to BL stimulation or darkness. Scale bars, 5
654 μm. **i,** Representative images (left) and quantification (right) of nigral TH^+ cells (blue)
655 and pS129 intensity (green) in the optoG4 mouse exposed to BL stimulation or darkness.
656 Low and high magnification scale bars, 200 and 20 μm, respectively. **j**, Motor function of
657 optoG4 mice exposed to BL stimulation or darkness in rotarod (left) and beam-walking
658 (right) tasks. Data are presented as mean ± standard error of mean. $*P < 0.05$ and $**P <$
659 0.01 by one-way (**f** sEPSC amplitude and frequency, and two-way (**f** (cumulative
660 probability of sEPSC amplitude and inter-event interval), and **j**) analysis of variance with
661 Bonferroni's multiple comparisons test and two-sided, unpaired Student's *t*-test (**i**).
662 Number of replicates is shown in Supplementary Table 9.
663

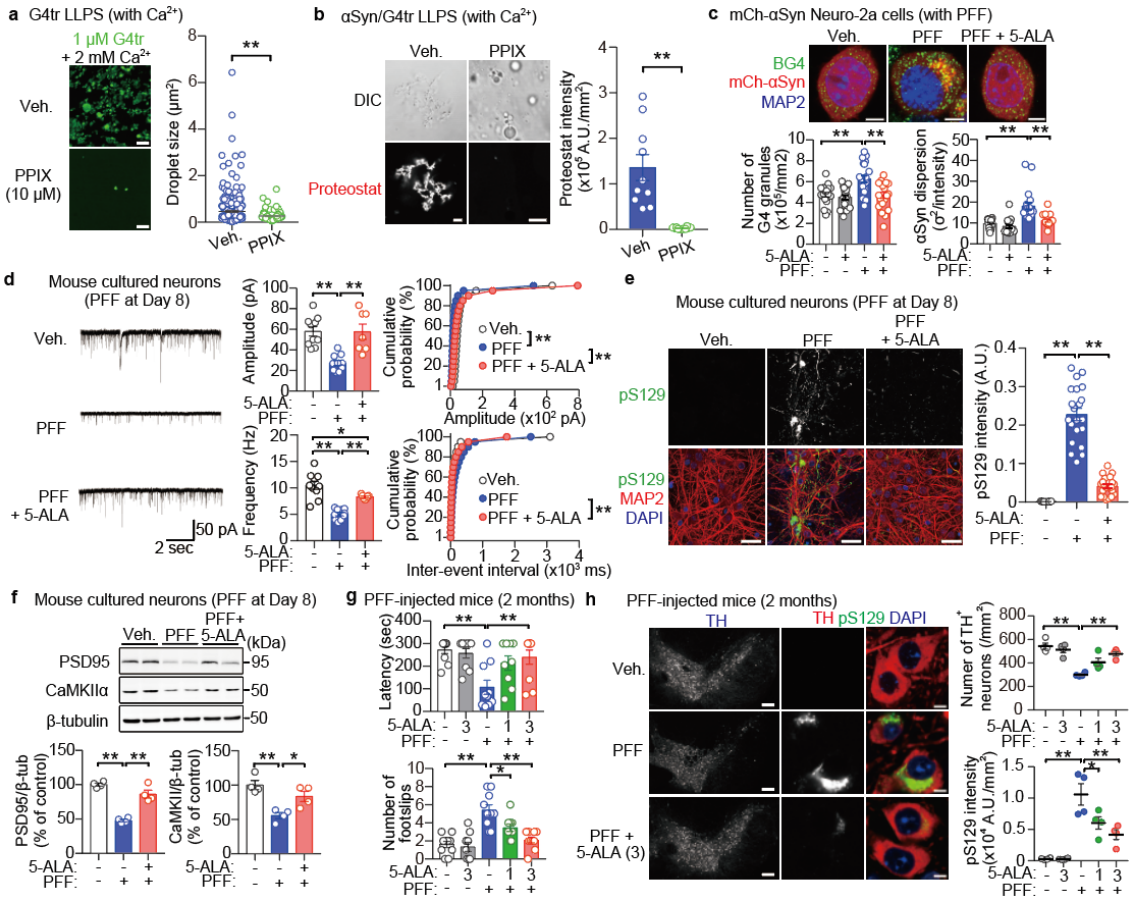

Fig. 5: G4 ligand ameliorates neuronal dysfunction by preventing α-synuclein (αSyn) aggregation.

a, Representative images (left) and quantification of droplet size (right) of *in vitro* phase-separated G4tr dependent on Ca^{2+} and the effect of protoporphyrin IX (PPIX). Scale bar, 5 μm. **b**, Proteostat intensity within *in vitro* phase-transitioned G4tr/αSyn dependent on Ca^{2+} and the effect of PPIX. Scale bar, 5 μm. **c**, Representative images (top) and quantification (bottom) of the number of G4 granules (green) and the dispersion of αSyn (red) in PFF-treated mCh-αSyn-expressing Neuro-2a cells and the effects of 3μM 5-aminolevulinic acid (5-ALA). Scale bars, 5 μm. **d**, Measurements of the spontaneous excitatory postsynaptic currents (sEPSCs) in PFF-treated mouse cultured neurons and the effects of 3 μM 5-ALA. **e**, Representative images (left) and quantification (right) of pS129 immunoreactivity (green) relative to $MAP2^{+}$ area (red) in pre-formed fibrils (PFF)-treated mouse cultured neurons and the effect of 3 μM 5-ALA. Scale bars, 20 μm. **f**, Representative images (top) and quantification (bottom) of immunoblots probed with the indicated antibodies in PFF-treated mouse cultured neurons and the effects of 5-ALA. **g**, Motor function of PFF-injected mice and the effects of 5-ALA in the rotarod (top) and beam-walking (bottom) tasks. **h**, Representative images (left) and quantification (right)

of the number of nigral tyrosine hydroxylase (TH^+) cells (red) and pS129 intensity (green) relative to the TH^+ area of PFF-injected mice and the effects of 5-ALA. Low and high magnification scale bars, 200 and 10 μm, respectively. Data are presented as mean ± standard error of mean. *$P < 0.05$ and **$P < 0.01$ by two-way (**d** (cumulative probability of sEPSC amplitude and inter-event interval)) and one-way (**c**,**d**,**e** (sEPSC amplitude and frequency),**f**,**g,h**) analysis of variance with Bonferroni's multiple comparisons test and by unpaired two-sided, unpaired Student's *t*-test (**a**,**b**). Number of replicates is shown in Supplementary Table 9.

690 **Methods**

691 **Animals**

692 C57BL/6J mice (Japan SLC) were used for all the experiments. Mice were
693 housed under climate-controlled conditions in a 12-hour light/12-hour dark cycle and
694 were provided standard food and water *ad libitum*. Animal studies were conducted in
695 accordance with the Kumamoto University institutional guidelines. Ethical approval was
696 obtained from the Institutional Animal Care and Use Committee of the Kumamoto
697 University Environmental and Safety Committee.

698

699 **Cell culture**

700 Neuro-2A and HEK293T cell lines were grown in Dulbecco's modified essential
701 medium (Sigma-Aldrich) containing 10% fetal bovine serum (FBS; Gibco), 100 units/mL
702 penicillin, and 100 μg/mL streptomycin at 5% CO_2 and 37°C. Transfection was performed
703 using the Lipofectamine 3,000 Reagent (Invitrogen) according to the manufacturer's
704 protocol. Primary cultures of mouse neurons were performed as previously described[9].
705 Briefly, cortical brain tissue was dissected from 18 days old embryonic mice, trypsin-
706 digested, and mechanically dispersed. Cells were seeded with minimum essential medium
707 (Gibco) supplemented with 10% FBS, 0.6% glucose (FUJIFILM), and 1 mM pyruvate
708 (Sigma-Aldrich). Cells were cultured in Neuron Culture Medium (FUJIFILM) with
709 medium changed every three days. Transfection was performed by electroporation
710 (NEPAGENE) or Magnetofection (OZ Biosciences) according to the manufacturer's
711 protocol.

712

713 **Plasmid constructs**

714 For protein purification, αSyn constructs with mouse coding sequence (CDS),
715 mutations, and CDS of fluorescent proteins were subcloned into pET-human αSyn[51] using
716 the KOD-Plus Mutagenesis kit (TOYOBO) and In-Fusion HD Cloning Kit (Takara Bio)
717 according to the manufacturers' protocol. For preparing the mammalian expression
718 plasmids, pCAG-GFP[9], pHR-FUSN-mCh-Cry2WT (Addgene #101223), and MCP-YFP
719 (Addgene #101160) were used as backbones. Repeat sequences of $(TTAGGG)_{23}$ and
720 $(TTACCG)_{23}$ were synthesized by GeneScript and subcloned into pHR-Tre3G-
721 29×GGGGCC-12×MS2 (Addgene #99149) using Ligation high (TOYOBO). The
722 fragments with MS2 were inserted in the 3'-untranslated region of pCAG-HaloTag vector[9].
723 For recombinant AAV production, pAAV-TH-iCre, pAAV-hSyn-DIO-MCP-Cry2, pAAV-
724 hSyn-G4tr-MS2, and pAAV-hSyn-G4mt-MS2 were synthesized by GeneScript, using
725 pAAV-hSyn-DIO{ChETA-mRuby2}on-W3SL (Addgene #111389) as a backbone.

726
727 **Antibodies**
728 The primary and secondary antibodies for immunoblotting and
729 immunohistochemical analyses utilized in the present study are shown in the
730 Supplementary Method.
731
732 **Preparation of recombinant proteins**
733 pET-αSyn plasmids were transformed into *Escherichia coli* BLR (DE3) cells and
734 purified as described previously[52]. Briefly, bacterial lysate by ultrasonication was heated
735 (75°C, 15 min) and precipitated by ammonium sulfate. The dialysate was fractionated by
736 ion exchange chromatography (Resource-Q or HiTrap SP HP; GE Healthcare) on an
737 AKTA-explorer system (GE Healthcare) at 4°C. Samples were desalted, lyophilized, and
738 stored at 4°C until the assay was conducted.
739
740 **Preparation of αSyn PFF**
741 αSyn PFF was prepared as previously described[51]. Briefly, recombinant αSyn (5
742 mg/mL in 1× phosphate buffer saline (PBS)) was centrifuged for an hour at 100,000g at
743 4°C and the supernatants were shaken in an orbital thermomixer at 1,000 rpm for seven
744 days. αSyn PFFs were sonicated by Bioruptor (Cosmo Bio) for eight cycles at high power
745 (on, 1-pulse every other second for 15 s in total; off, 15 s; at 23°C), and then stored at -
746 80°C until use.
747
748 **AAV preparation**
749 Recombinant AAV9 vectors were generated by co-transfection of AAVpro 293T
750 cells (Takara Bio) with three plasmids: pAAV, pHelper (Stratagene), and pAAV2/9 (a gift
751 from James M. Wilson). The viral particles were purified from transfected cells and
752 titrated using the AAVpro Purification Kit Maxi and AAVpro Titration Kit (Takara Bio)
753 according to the manufacturer's instructions.
754
755 **Treatment with αSyn PFF and other compounds in cultured cells**
756 Neuro-2a or HEK293T cells expressing mCh- or GFP-human αSyn were treated
757 with human αSyn PFF at 50 μg/mL (3.45 μM) for the indicated time. Mouse cultured
758 neurons at DIV10 were incubated with mouse or human αSyn PFF at 50 μg/mL for the
759 indicated time, some of which were further treated with 5 μM Calbryte 520AM (AAT
760 Bioquest) for 30 min. Several mouse cultured neurons were treated with 0.5 mM $NaAsO_2$
761 (Sigma-Aldrich) for 60 min or 1.0 μM ionomycin (AdipoGen Life Sciences) for 30 min

762 on DIV14.
763
764 **Intracellular Ca^{2+} imaging**
765 αSyn PFF- and Calbryte 520AM-treated mouse cultured neurons were subjected
766 to measurement of intracellular Ca^{2+} levels using LSM900 microscopy system (Carl
767 Zeiss) in an imaging chamber (KYODO INTERNATIONAL).
768
769 **Stereotaxic injection of αSyn PFF and AAV**
770 Mouse αSyn PFFs were injected into the bilateral dorsal striatum (2
771 μg/hemisphere) at the following coordinates (in mm): anterior, +0.7; lateral, ±2.5; and
772 depth, -2.8 relative to the bregma. Viral particles of 1-μL with the same titer (1.4×10^{10}
773 vector genomes/mL) were injected into the bilateral substantia nigra at the following
774 coordinates (in mm): anterior, -3.5; lateral, ±1.2; and depth, -4.0 relative to the bregma.
775 αSyn PFFs and AAV were injected at 0.2 μL/min using a Hamilton syringe under 1%
776 isoflurane anesthesia.
777
778 **FRAP assay in living cells**
779 GFP-αSyn-transfected and αSyn PFF-transduced HEK293T cells were subjected
780 to FRAP assay in the imaging chamber. Fluorescent images were obtained using the
781 LSM900 microscopy system. Photobleaching was performed with 50% laser power with
782 20 iterations. Time-lapse images were recorded every 250 ms at room temperature.
783
784 ***In vitro* LLPS, Proteostat, and FRAP assay**
785 Non-labeled or mCh-labeled human αSyn (34.5 or 69 μM) was prepared in the
786 LLPS assay buffer: 50 mM Tris-HCl buffer (pH 7.5) containing 140 mM KCl, 15 mM
787 NaCl, 10 mM $MgCl_2$, 0–20% PEG8000 (MP Biomedicals), and 1 unit/μL RNase inhibitor
788 (TOYOBO) in the presence or absence of 2 mM $CaCl_2$ and 2.5 mM EGTA. Total protein,
789 total RNA, or synthesized 24-mer RNA oligomer (1 μM; Hokkaido System Science) was
790 added and incubated at 37°C for three hours. Total protein was lysed by homogenization
791 in radioimmunoprecipitation (RIPA) buffer (FUJIFILM) containing protease inhibitor
792 cocktail (NACALAI TESQUE) and Cryonase Cold-active Nuclease (TAKARA), while
793 total RNA was extracted using an RNeasy Mini Kit (Qiagen), both from intact Neuro-2a
794 cells. The resultant solutions were mounted on glass slides using a 0.12 nm spacer
795 (Sigma-Aldrich) and a coverslip. In some conditions, 2% (v/v) Proteostat reagent (Enzo
796 Life Sciences) was added into the LLPS assay buffer to detect aggregates. Differential
797 interference contrast images were obtained using the TCS SP8 confocal microscopy

798 system (Leica Microsystems). Samples were photobleached with 50% laser power and
799 time-lapse images were recorded every 8-s using the LSM780 microscopy system.
800
801 **Circular dichroism (CD) spectroscopy**
802 G4tr $(UUAGGG)_4$ and G4mt $(UUACCG)_4$ were prepared using an *in vitro* the
803 HiScribe T7 Quick High Yield RNA Synthesis Kit (New England Biolabs) following the
804 manufacturers' instructions, respectively. Other RNA oligomers were synthesized by
805 Hokkaido System Science. Each RNA (2.5 μM) was prepared in 10 mM Tris-HCl buffer
806 (pH 7.5) containing 100 mM LiCl or KCl. The oligomers were then refolded by a
807 heating/cooling process (90°C for 3 min, followed by cooling down to 10°C for 1.5 hours)
808 before measurement. The CD spectra were recorded at room temperature over the range
809 of 200–350 nm using a spectrometer (J-805LST; JASCO) equipped with a 3 mm path-
810 length quartz cuvette.
811
812 **EMSA**
813 Fluorescein phosphoramidite (FAM)-labeled RNAs (20 nM) in 10 mM Tris-HCl
814 buffer (pH 7.5) containing 100 mM NaCl were refolded as described above. The folded
815 RNA samples were incubated with a human αSyn (0–138.4 μM) or BG4 (320 nM) with
816 1 unit/μL RNase inhibitor (TOYOBO) at room temperature for at least 30 min. The
817 resulting mixtures were analyzed by 6% native TBE polyacrylamide gel electrophoresis
818 and visualized using Typhoon Trio equipment (GE Healthcare).
819
820 **SPR-binding assays**
821 SPR experiments were performed on OpenSPR (Nicoya). After biotin-labeled
822 G4tr or G4mt was captured by a sensor chip using biotin-streptavidin sensor kit (Nicoya),
823 αSyn in running buffer (50 mM Tris-HCl pH 7.5 and 10 mM KCl) was streamed over the
824 sensor chip to allow interaction. The interaction time was at least 5 min to allow the ligand
825 signal to stabilize. The running buffer was then flowed at a rate of 20 μL/min for 5 min
826 to collect the dissociation data. Binding kinetic parameters were obtained by fitting the
827 curve to a One-to-One binding model using TraceDrawer software (Ridgeview
828 Instruments).
829
830 **RNA Bind-n-Seq**
831 RNA Bind-n-Seq was performed as previously described[30]. Briefly, the purified
832 αSyn (0–69 μM) and BG4 (0.32 μM) were equilibrated in binding buffer (25 mM Tris-
833 HCl pH 7.5, 150 mM KCl, 3 mM $MgCl_2$, 0.01% Tween 20, 1 mg/ml bovine serum

834 albumin (BSA), and 1 mM dithiothreitol) with 1 units/μL RNase inhibitor (TOYOBO)
835 for 30 min at room temperature. 24-mer random RNAs of 1 μM (Hokkaido System
836 Science) were added to the solutions and incubated for an hour at 4°C. During the
837 incubation, Dynabeads Protein G (Invitrogen) was washed with wash buffer (25 mM Tris-
838 HCl pH 7.5, 150 mM KCl, 60 μg/mL BSA, 0.5 mM EDTA, and 0.01% Tween 20) and
839 then equilibrated in binding buffer including 1 units/μL RNase inhibitor with anti-αSyn
840 or anti-DYKDDDDK tag antibody until use. The protein/RNA complex was pulled down
841 by the beads and incubated for an hour at room temperature. Supernatant was removed
842 and the beads were washed once. The beads were incubated at 70°C for 10 min in elution
843 buffer (10 mM Tris-HCl pH 7.0, 1% sodium dodecyl sulfate (SDS), and 1 mM EDTA).
844 Bound RNA was extracted and reverse-transcribed into cDNA using Superscript III
845 (Invitrogen) according to the manufacturer's instructions together with the following
846 primer: 5'-GCCTTGGCACCCGAGAATTCCA-3'. To control for any nucleotide biases
847 in the input random library, the input RNA pool (0.5 pmol) was also reverse-transcribed
848 and Illumina sequencing library prep was followed by 8–10 cycles of polymerase chain
849 reaction (PCR) using High Fidelity Phusion (New England Biolabs). All the libraries were
850 barcoded in the PCR step, pooled together, and sequenced on a NextSeq 500 sequencer.
851 Motif enrichment analyses were performed by the MERMADE program[53]. Base contents,
852 GC contents, and GC skew were calculated by the SeqKit program[54]. The motifs were
853 processed by enoLOGOS21 (http://www.benoslab.pitt.edu/cgi-
854 bin/enologos/enologos.cgi), and putative G4 sequences were predicted using QuadBase2
855 (https://quadbase.igib.res.in/).
856
857 **RIP-seq**
858 Immunoprecipitation of RNPs was performed using a RiboCluster Profiler RIP-
859 Assay kit for microRNA (MBL) according to the manufacturer's protocol. Cells were
860 harvested, lysed, and precleared on Dynabeads Protein G for an hour at 4°C. The
861 precleared lysates were incubated at 4°C for three hours in the beads immobilized with
862 normal rabbit IgG, anti-αSyn, or BG4 with anti-DYKDDDDK tag antibody. Each fraction
863 containing protein-bound RNA was purified and prepared for RNA-sequencing library
864 using NEBNext Ultra II Directional RNA Library Prep Kit for Illumina (New England
865 Biolabs). All the libraries were sequenced on a NextSeq 500 sequencer (Illumina). Fastq
866 files were processed for quality check and adapter trimming with the Trimgalore! (v0.6.6).
867 Trimmed reads were used for mapping the mouse genome (mm10) using the STAR
868 (v2.7.9a). DESeq2(v1.38.3) was used for identifying BG4-enriched transcripts. Putative
869 rG4-forming motifs of mRNAs were predicted using the QGRS mapper

870 (http://bioinformatics.ramapo.edu/QGRS/index.php). GO analysis was performed using
871 DAVID Bioinformatics Resources (https://david.ncifcrf.gov/home.jsp).
872
873 **Photoactivation by exposure of BL stimulation**
874 For live cell imaging, OptoG4-expressing Neuro-2a cells were placed in the
875 imaging chamber and imaged typically with two laser wavelengths (488 nm for Cry2olig
876 photoactivation/560 nm for mCh imaging) using the LSM780 microscopy system.
877 Cry2olig photoactivation was induced at 5% power and time-lapse acquisitions were
878 performed every 20 s at room temperature. For electrophysiological and
879 immunohistochemical analyses, cells were photoactivated using 470 nm blue light-
880 emitting diode (LED) light (Bio Research Center) with an estimated light intensity of
881 1.0 mW/cm^2. For *in vivo* photoactivation, mice were implanted with dual-LED optic
882 cannulae at 470 nm (Bio Research Center) into the bilateral substantia nigra two weeks
883 following AAV injection. Daily photoactivation was performed using Teleopto, a wireless
884 optogenetic stimulation system (Bio Research Center).
885
886 **Drugs**
887 PPIX was purchased from Sigma-Aldrich. 5-ALA hydrochloride and sodium
888 ferrous citrate were provided by SBI Pharmaceuticals. PPIX (10 μM) was added to the
889 LLPS assay buffer. Cultured cells were co-treated with PFF and 5-ALA (3 μM with
890 sodium ferrous citrate [20:1 molar ratio] dissolved in sterilized distilled water) or vehicle
891 (sodium ferrous citrate). Animals were orally administered with vehicle or 5-ALA (1 or
892 3 mg/kg/day) with sodium ferrous citrate 24 hours following αSyn PFF injection daily
893 for two months.
894
895 **Electrophysiology**
896 sEPSC was recorded at room temperature for mouse cultured neurons on DIV14
897 (optoG4) or DIV18 (αSyn PFF) using an EPC10 amplifier (HEKA Instruments) as
898 previously described[9]. The following buffers were used in the present study: extracellular
899 buffer (143 mM NaCl, 5 mM KCl, 2 mM $CaCl_2$, 1 mM $MgCl_2$, and 10 mM glucose, and
900 10 mM HEPES at pH 7.4 adjusted with NaOH) and intracellular buffer (135 mM CsMeS,
901 5 mM CsCl, 0.5 mM EGTA, 1 mM $MgCl_2$, 4 mM Mg_2ATP, 0.4 mM NaGTP, 5 mM QX-
902 314 and 10mM HEPES at pH 7.4 adjusted with CsOH). Recording pipettes had a
903 resistance of 3.5–4.5 MΩ when filled with the intracellular buffer. The sEPSC was
904 recorded for 2 min at a holding potential of -70 mV in the presence of 10 μM bicuculline
905 in the extracellular buffer. Recordings were filtered at 2 kHz and digitized at 10 kHz. Data

906 were collected and initially analyzed using Patchmaster software (HEKA). Further
907 analysis was performed using SutterPatch v2.2 (Sutter Instrument).
908
909 **Immunohistochemical analysis**
910 Immunohistochemistry was performed as previously described[9]. Cells and
911 mouse brain slices (50 μm thickness) were fixed with 4% paraformaldehyde, washed with
912 1× PBS, permeabilized with 0.1–0.3% Triton X-100, and incubated with 1% BSA and
913 0.1–0.3% Triton X-100 in 1× PBS. Human frozen brain sections (5–10 μm thickness)
914 were obtained from BioChain Institute and a part of them were treated with RNase A. An
915 hour after blocking, samples were treated with primary antibodies for 1–3 days at 4°C.
916 After incubation with fluorophore-conjugated secondary antibodies, samples were
917 mounted in Vectashield (Vector Laboratories). Some samples were counterstained with
918 4',6-diamidino-2-phenylindole. Immunofluorescence images were obtained using
919 LSM900 or TCS SP8 confocal microscopy system.
920
921 **Fluorescent *in situ* hybridization (FISH)**
922 FISH was performed as previously described[9]. After permeabilization as
923 described above, the samples were prehybridized with hybridization solution (2× saline-
924 sodium citrate (SSC), 40% formamide, 10% dextran sulfate, 2 mM vanadyl sulfate, 0.5
925 mg/mL yeast transfer RNA) for 60 min at 37 (*MS2*) or 60°C (*Camk2a* and *Dlg4*), and
926 then incubated with 1 nM (*MS2*) or 0.3 μM (*Camk2a* and *Dlg4*) probe in a hybridization
927 solution at 37 or 60°C overnight. After hybridization, samples were washed and subjected
928 to immunofluorescence procedures and images were collected as described above. FISH
929 probe sequences are shown in the Supplemental Method.
930
931 **Western blotting analysis**
932 Western blot analyses were performed as previously described[9]. Briefly, primary
933 mouse cultured neurons were homogenized in RIPA buffer with a protein inhibitor
934 cocktail. The lysate was centrifuged and protein concentration of the supernatant was
935 determined by BCA method, and samples were then boiled for 3 min in Laemmli's sample
936 buffer. Equal amounts of protein were loaded onto SDS-polyacrylamide gels. After
937 transferring the separated proteins to polyvinylidene difluoride membranes, the
938 membranes were blocked with 5% non-fat skim milk and incubated with primary
939 antibody at 4°C overnight. Blots were developed using an ECL Western Blotting
940 Substrate (Thermo Scientific), and the signals were detected using LAS-4000mini (GE
941 Healthcare).

942

943 **Quantitative PCR with reverse transcription (RT-qPCR)**

944 Sample preparation for RT-qPCR from primary cultured neurons was performed
945 using the RNeasy Mini Kit and PrimeScript RT Master Mix (Takara Bio). RT-qPCR was
946 performed using KOD SYBR qPCR Mix (TOYOBO) on a CFX Connect Real-Time PCR
947 System (Bio-Rad Laboratories). Gene expression was assessed using the differences in
948 normalized Ct (cycle threshold) ($^{\Delta\Delta}$Ct) method after normalization to *Gapdh* expression.
949 Fold change was calculated by $2^{-\Delta\Delta Ct}$. PCR primers are shown in the Supplemental
950 Method.

951

952 **Behavioral analysis**

953 The rotarod and beam-walking tasks were performed according to a previous
954 report[51]. Briefly, mice were trained before the stereotaxic injection. In the rotarod task,
955 mice were placed on the rod rotating at 20 rpm and falling latency was measured for up
956 to 5 min. In the beam-walking task, the number of foot-slips from the end of beam to goal
957 box was recorded.

958

959 **Statistical analysis**

960 Data are presented as the mean ± standard error of the mean. Comparisons
961 between two experimental groups were made using unpaired Student's t-test. Statistical
962 significance for differences among groups was tested by one-way or two-way analysis of
963 variance with *post-hoc* Bonferroni's multiple comparison test. $P < 0.05$ represented a
964 statistically significant difference. All the statistical analyses were performed using
965 GraphPad Prism 7 (GraphPad Software). Source data are provided in Supplementary
966 Table 9.

967

968 **Methods references**

969

970 51. Yabuki, Y. et al. Fatty Acid Binding Protein 3 Enhances the Spreading and Toxicity
971 of α-Synuclein in Mouse Brain. *Int. J. Mol. Sci.* **21**, 2230 (2020).

972

973 52. Izawa, Y. et al. Role of C-terminal negative charges and tyrosine residues in fibril
974 formation of α-synuclein. *Brain Behav.* **5**, 595–605 (2012).

975

976 53. Kashiwazaki, G. et al. Comparative Analysis of DNA-Binding Selectivity of Hairpin
977 and Cyclic Pyrrole-Imidazole Polyamides Based on Next-Generation Sequencing.
978 *Chembiochem*. **17**, 1752–1758 (2016).

979

980 54. Shen, W., Le, S., Li, Y., Hu, F. SeqKit: A Cross-Platform and Ultrafast Toolkit for
981 FASTA/Q File Manipulation. *PLoS One.* **11**, e0163962 (2016).

982

Acknowledgments

This work was supported by AMED (grant numbers: JP21wm0525023 and JP21gm6410021 to Y.Y.; JP22ek0109591 and JP23ek0109651 to N.S.), JSPS KAKENHI (grant numbers: JP21K20723 and JP22J00687 to K.Matsuo; JP21K06579 to Y.Y.; and JP21H00207, JP20K21400, and JP22K19297 and JP23H00373 to N.S.), JST FOREST Program (JPMJFR2043 to N.S.), The Pharmacological Research Foundation, Tokyo (to Y.Y.), Kowa Life Science Foundation (to Y.Y.), Narishige Neuroscience Research Foundation (to Y.Y.), the Astellas Foundation for Research on Metabolic Disorders (to N.S.), the Foundation of SBI Pharmaceuticals Co., Ltd. (to N.S.), International Research Core for Stem Cell-based Developmental Medicine Encourage Project and The Inter-University Research Network for High Depth Omics, Institute of Molecular Embryology and Genetics, Kumamoto University.

Author information

Authors and Affiliations

Department of Genomic Neurology, Institute of Molecular Embryology and Genetics (IMEG), Kumamoto University, Kumamoto, Japan

Kazuya Matsuo, Sefan Asamitsu, Kohei Maeda, Kosuke Kawakubo, Ginji Komiya, Kenta Kudo, Yusuke Sakai, Karin Hori, Susumu Ikenoshita, Norifumi Shioda and Yasushi Yabuki

Center for Biosystems Dynamics Research (BDR), RIKEN, Kobe, Japan

Sefan Asamitsu

Graduate School of Pharmaceutical Sciences, Kumamoto University, Kumamoto, Japan.

Kohei Maeda, Kosuke Kawakubo, Ginji Komiya, Kenta Kudo, Yusuke Sakai, Norifumi Shioda and Yasushi Yabuki

Liaison Laboratory Research Promotion Center, Institute of Molecular Embryology and Genetics (IMEG), Kumamoto University, Kumamoto, Japan.

Shingo Usuki

Department of Chemistry and Biotechnology, Graduate School of Engineering Tottori University, Tottori, Japan

Shiori Funahashi, Yasushi Kawata, Tomohiro Mizobata

Author Contributions

N.S. and Y.Y. designed the study. K.Matsuo, S.A., K.Maeda, K.Kawakubo, G.K., K.Kudo, Y.S., K.H., S.I., S.U., S.F., and Y.Y. performed the experiments. Y.K. and T.M. provided critical advice for αSyn synthesis and analysis of the interaction between rG4 and αSyn. K.Matsuo, N.S., and Y.Y. wrote the manuscript. N.S. and Y.Y. supervised the project.

Corresponding author

Correspondence should be addressed to Norifumi Shioda and Yasushi Yabuki.

Competing interests

The authors declare that they have no competing interests.

Data Availability

The raw data of RNA-Bind-n-Seq and RIP-Seq analyses are available at Gene Expression Omnibus (accession number: GSE235418 and GSE234238, respectively). Additional data related to this paper may be requested from the corresponding author N.S. and Y.Y. upon reasonable request.

Supplementary Information is available for this paper

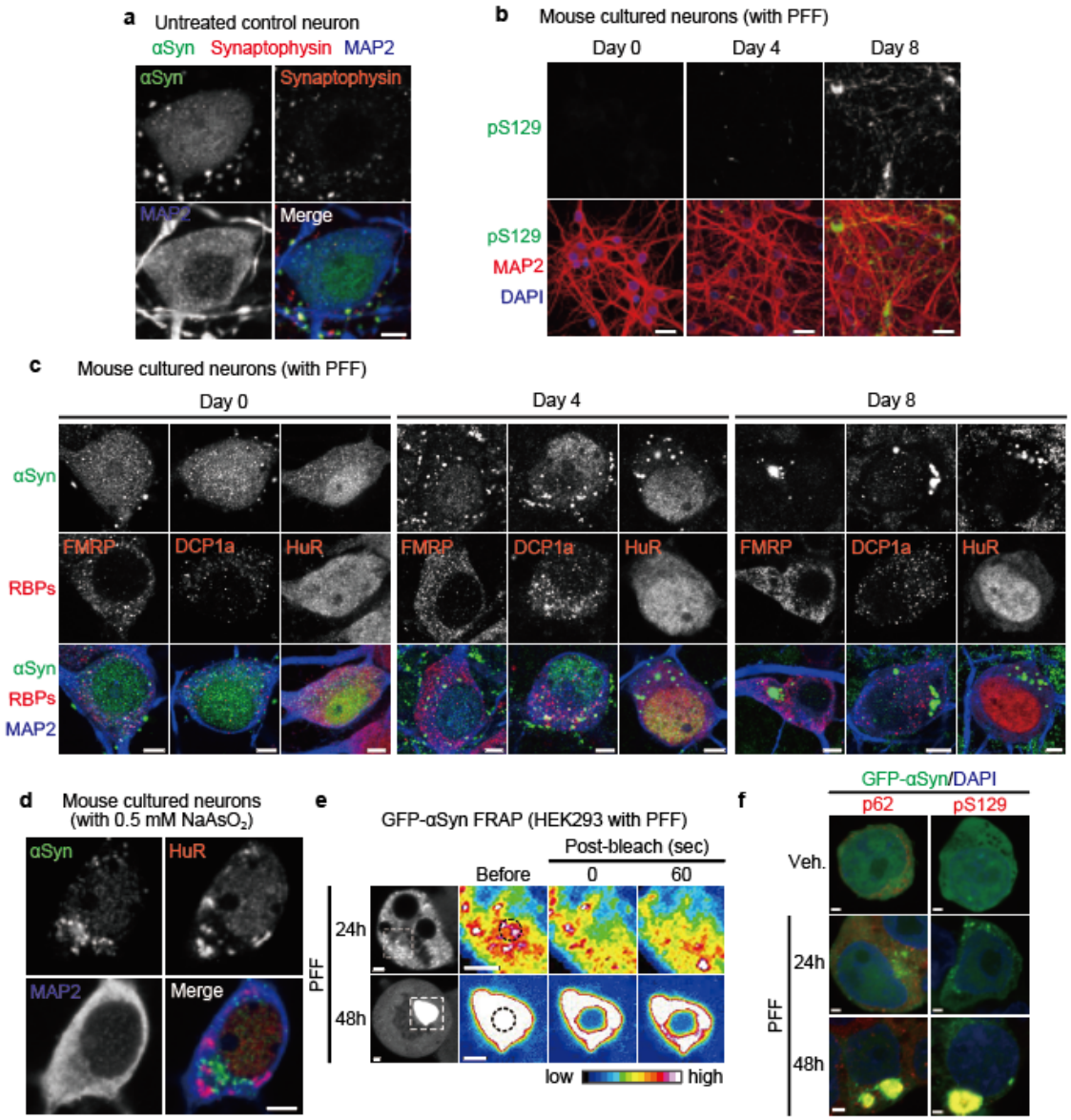

Extended Data Fig. 1: Localization and dynamics of α-synuclein (αSyn) under cellular stress.

a, Representative images of αSyn (green), synaptophysin (red), and MAP2 (blue) in naïve mouse cultured neurons. Scale bar, 5 μm. **b**, Representative images of pS129 (green), MAP2 (red), and 4',6-diamidino-2-phenylindole (DAPI) (blue) in mouse cultured neurons following pre-formed fibrils (PFF) treatment for the indicated time. Scale bars, 20 μm. **c**, Representative images of αSyn (green), RNA binding proteins (red), and MAP2 (blue) in mouse cultured neurons after PFF treatment for the indicated time. Scale bars, 5 μm. **d**, Representative images of αSyn (green), HuR (red), and MAP2 (blue) in mouse cultured neurons after treatment with 0.5 mM $NaAsO_2$ for 60 min. Scale bar, 5 μm. **e,** Representative images of αSyn fluorescence recovery after photobleaching assay in PFF-

1050 treated GFP-αSyn expressing HEK293T cells. Scale bars, 2 μm. **(f)**, Representative
1051 images of p62 or pS129 (red) and DAPI (blue) in HEK293T cells treated with PFF
1052 following GFP-αSyn overexpression (green). Scale bars, 2 μm.
1053

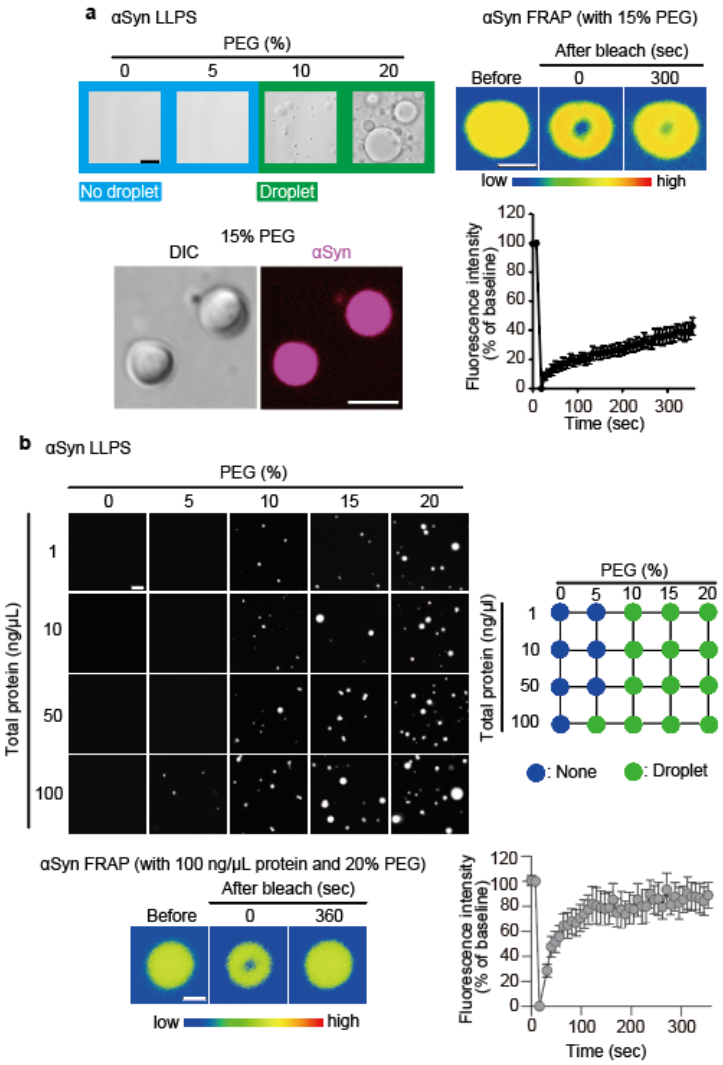

Extended Data Fig. 2: *In vitro* α-synuclein (αSyn) phase separation in the presence of a molecular crowding agent.

a, *In vitro* αSyn phase separation (left) and fluorescence recovery after photobleaching (FRAP) assay (right) dependent on polyethylene glycol (PEG). Scale bars, 5 (Differential interference contrast image) and 2 (Fluorescent images) μm, respectively. **b**, *In vitro* αSyn phase separation (top) and FRAP assay (bottom) dependent on PEG and total protein extracted from Neuro-2a cells. Data are presented as mean ± standard error of mean. n = 7 (**a**) and n = 7 (**b**).

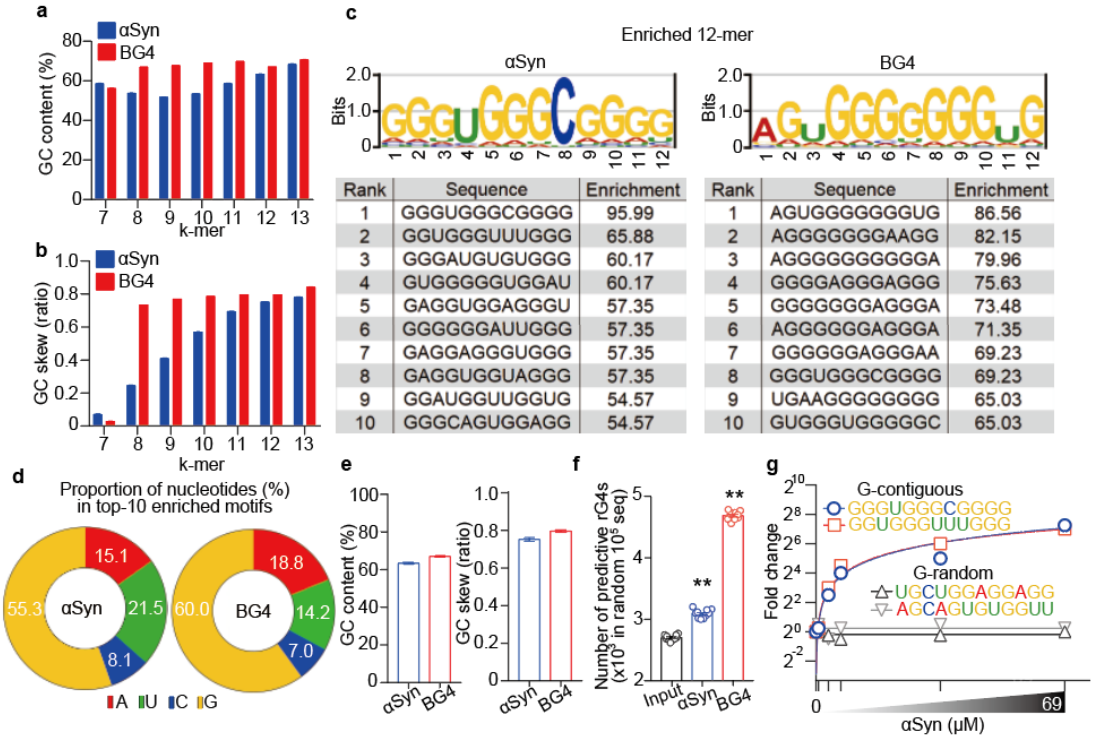

Extended Data Fig. 3: Analysis of RNA Bind-n-Seq for α-synuclein (αSyn). **a**,**b**, GC contents (**a**) and GC skew (**b**) in *k*-mer sequences in enriched motifs for αSyn and BG4. **c**–**e**, The top 10 motifs enriched in αSyn and BG4 (**c**), the proportion of nucleotides (**d**), and the GC contents and GC skew (**e**). **f**, Number of sequences with predicted rG4 structures enriched in αSyn and BG4. **g**, Fold enrichment of the top two 12-mers (circle and square marks) and two randomly chosen 12-mers (triangle marks) across αSyn concentrations (see legends in **Fig. 1f**). Data are presented as mean ± standard error of mean. $^{**}P < 0.01$ by one-way analysis of variance with Bonferroni's multiple comparisons test. Number of replicates is shown in Supplementary Table 9.

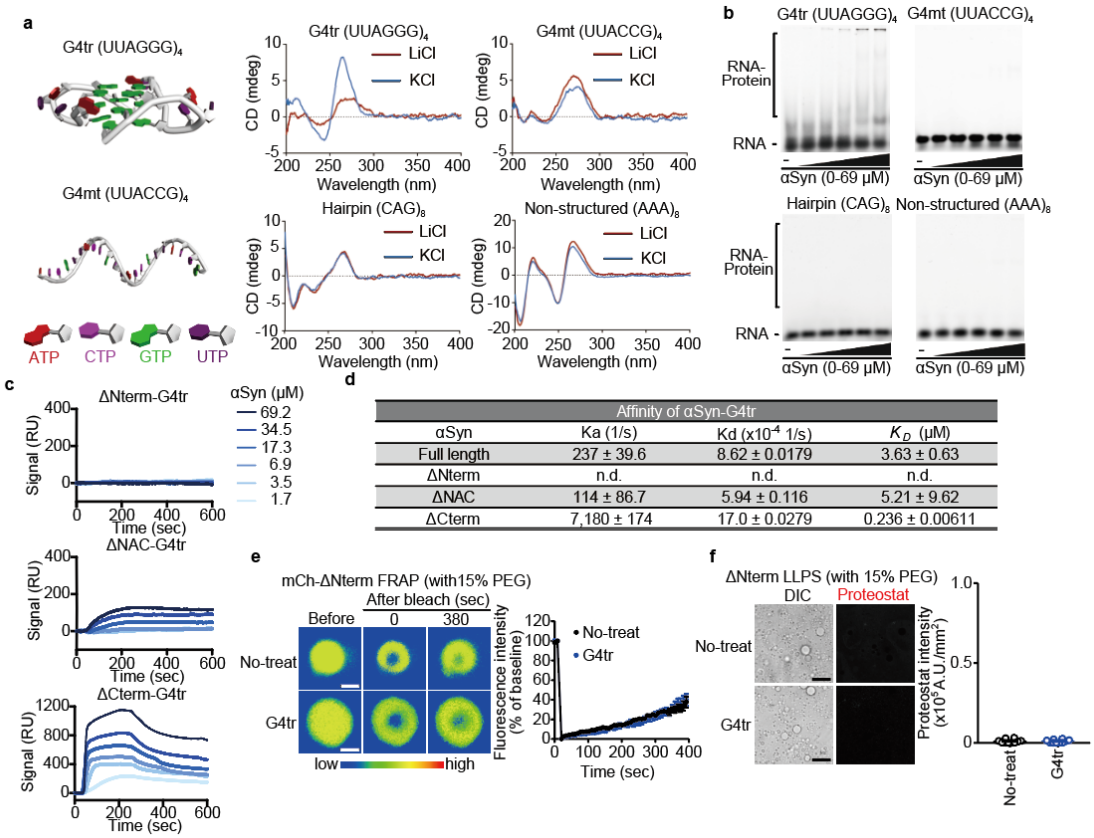

Affinity of αSyn-G4tr			
αSyn	Ka (1/s)	Kd (x10^{-4} 1/s)	K_D (μM)
Full length	237 ± 39.6	8.62 ± 0.0179	3.63 ± 0.63
ΔNterm	n.d.	n.d.	n.d.
ΔNAC	114 ± 86.7	5.94 ± 0.116	5.21 ± 9.62
ΔCterm	7,180 ± 174	17.0 ± 0.0279	0.236 ± 0.00611

Extended Data Fig. 4: Physicochemical and biochemical analyses of RNA structures interacting to α-synuclein (αSyn).

a, Schematic illustration of G4tr and G4mt (left). Circular dichroism spectra of the indicated RNAs in the presence of 100 mM KCl or LiCl (right). **b**, Representative images of electrophoresis mobility shift assay for the interaction of αSyn (0, 0.69, 3.45, 6.9, 34.5, and 69 μM μM) with Fluorescein phosphoramidite-labeled G4tr, G4mt, $(CAG)_8$, or $(AAA)_8$ oligomers (20 nM) in the presence of 100 mM NaCl. **c**,**d**, Representative surface plasmon resonance binding curves (**c**) and the detailed parameters (**d**) related to the interaction of G4tr with αSyn ΔNterm, ΔNAC, and ΔCterm. K_D, dissociation constant; Ka, association rate constant; Kd, dissociation rate constant; n.d., not detected. **e**,**f**, *In vitro* G4tr/αSyn ΔNterm fluorescence recovery after photobleaching assay (**e**) and Proteostat intensity within the phase-separated droplets (**f**) dependent on 15% PEG. Scale bars, 1 (**e**) and 10 (**f**) μm, respectively. Data are presented as mean ± standard error of mean. Number of replicates is shown in Supplementary Table 9.

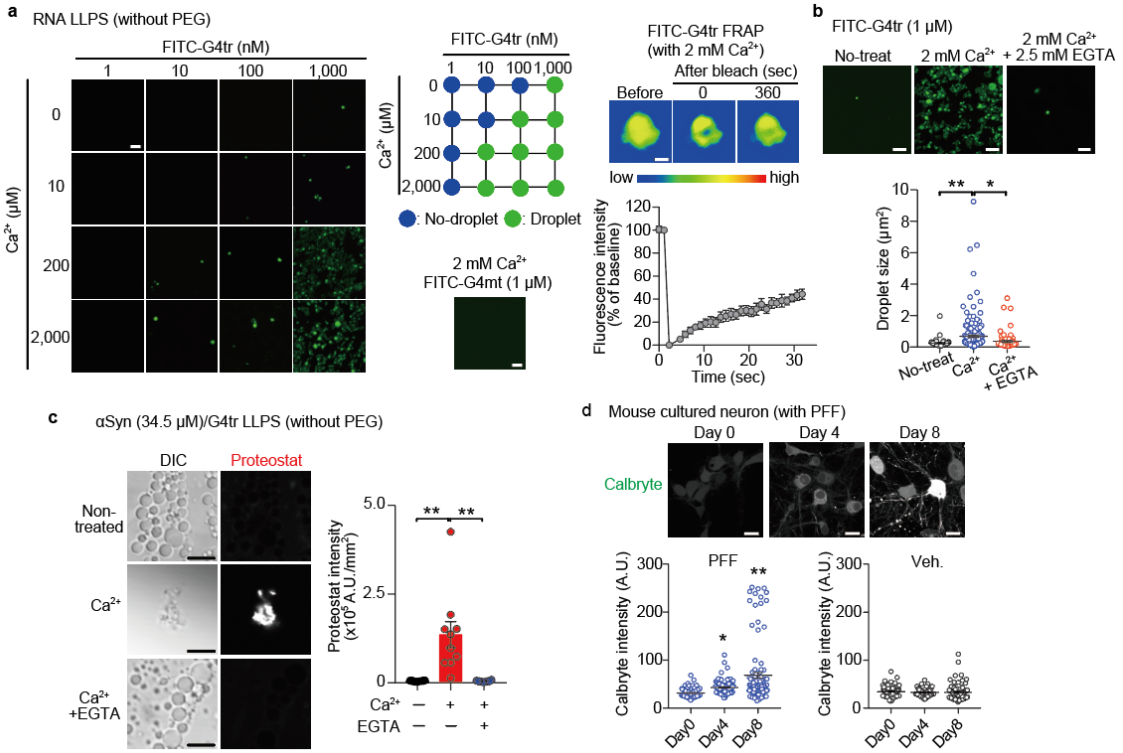

Extended Data Fig. 5: Ca^{2+}-dependent G4tr assembly promotes α-synuclein (αSyn) sol–gel phase transition.

a, *In vitro* G4tr and G4mt phase separation (left, center) and fluorescence recovery after photobleaching (FRAP) assay (right) dependent on Ca^{2+}. Scale bars, 5 μm. n = 5 (FRAP). **b**, Representative images (top) and quantification of droplet size (bottom) of *in vitro* phase-separated G4tr dependent on Ca^{2+} and the effect of EGTA. Scale bars, 5 μm. **c**, Representative images (left) and quantification (right) of Proteostat intensity within phase-transitioned G4tr/αSyn dependent on Ca^{2+}. Scale bars, 5 μm. **d**, Representative images (top) and quantification (bottom) of Calbryte 520AM intensity in mouse cultured neurons after PFF treatment for the indicated time. Scale bars, 20 μm. Data are mean ± s.e.m. $*P < 0.05$ and $**P < 0.01$ by one-way analysis of variance with Bonferroni's multiple comparisons test. Number of replicates is shown in Supplementary Table 9.

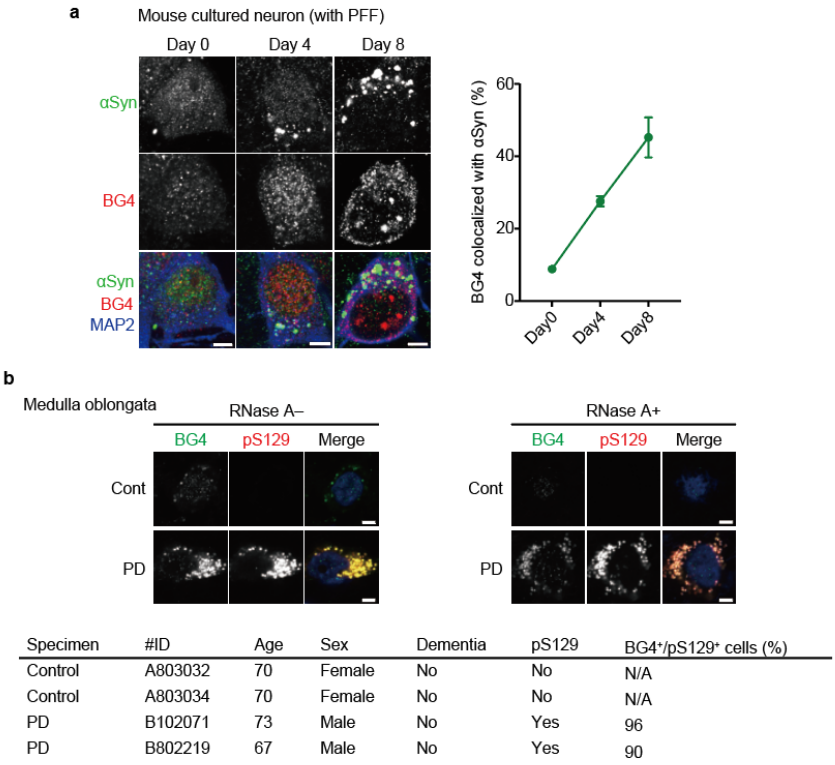

Specimen	#ID	Age	Sex	Dementia	pS129	BG4⁺/pS129⁺ cells (%)
Control	A803032	70	Female	No	No	N/A
Control	A803034	70	Female	No	No	N/A
PD	B102071	73	Male	No	Yes	96
PD	B802219	67	Male	No	Yes	90

Extended Data Fig. 6: Co-aggregation of RNA G-quadruplexes and α-synuclein (αSyn) in pre-formed fibrils (PFF)-treated mouse cultured neurons and postmortem brain of patients with Parkinson's disease.

a, Representative images (left) and quantification (right) of co-localization of αSyn (green) and BG4 (red) granules in MAP2^{+} cells (blue) in mouse cultured neurons after PFF treatment. n = 12 (day 0), 15 (day 4), and 8 (day 8). Scale bars, 5 μm. **b**, Representative images of BG4 (green), pS129 (red), and 4',6-diamidino-2-phenylindole (blue) in the medulla oblongata of human normal control and patients with PD treated with or without RNase A (top). Scale bars, 5 μm. Information for human samples and the proportion of BG4^{+} cells among pS129^{+} cells (bottom). Data are presented as mean ± standard error of mean.

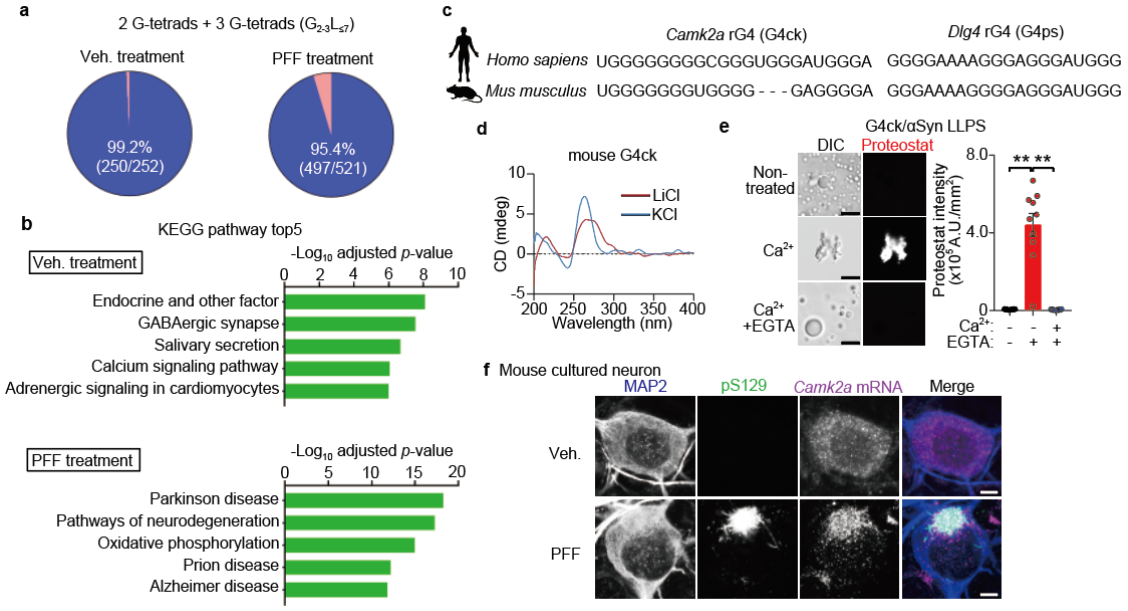

Extended Data Fig. 7: Bioinformatic and biophysical analyses of BG4-RIP-seq in pre-formed fibrils (PFF)-treated mouse cultured neurons.

a, RNA G-quadruplexes (rG4s) in BG4-enriched RNAs containing two or three G-tetrads ($G_{2-3}L_{\leq 7}$) predicted by quadruplex-forming guanine-rich sequences (QGRS) mapper in mouse cultured neurons after PFF treatment. **b**, Kyoto Encyclopedia of Genes and Genomes (KEGG) pathway analysis in BG4-enriched RNAs in mouse cultured neurons after PFF treatment. **c**,**d**, Predicted rG4 sequences in human/mouse G4ck and G4ps (**c**) and circular dichroism spectra of mouse G4ck in the presence of KCl or LiCl (**d**). **e**, Representative images (left) and quantification (right) of Proteostat intensity within phase-transitioned G4ck/αSyn dependent on Ca^{2+}. Scale bars, 5 μm. **f**, Representative images of MAP2 (blue), pS129 (green), and *Camk2a* RNA (magenta) in mouse cultured neurons after PFF treatment. Scale bars, 5 μm. Data are presented as mean ± standard error of mean. $^{**}P < 0.01$ by one-way analysis of variance with Bonferroni's multiple comparisons test. Number of replicates is shown in Supplementary Table 9.

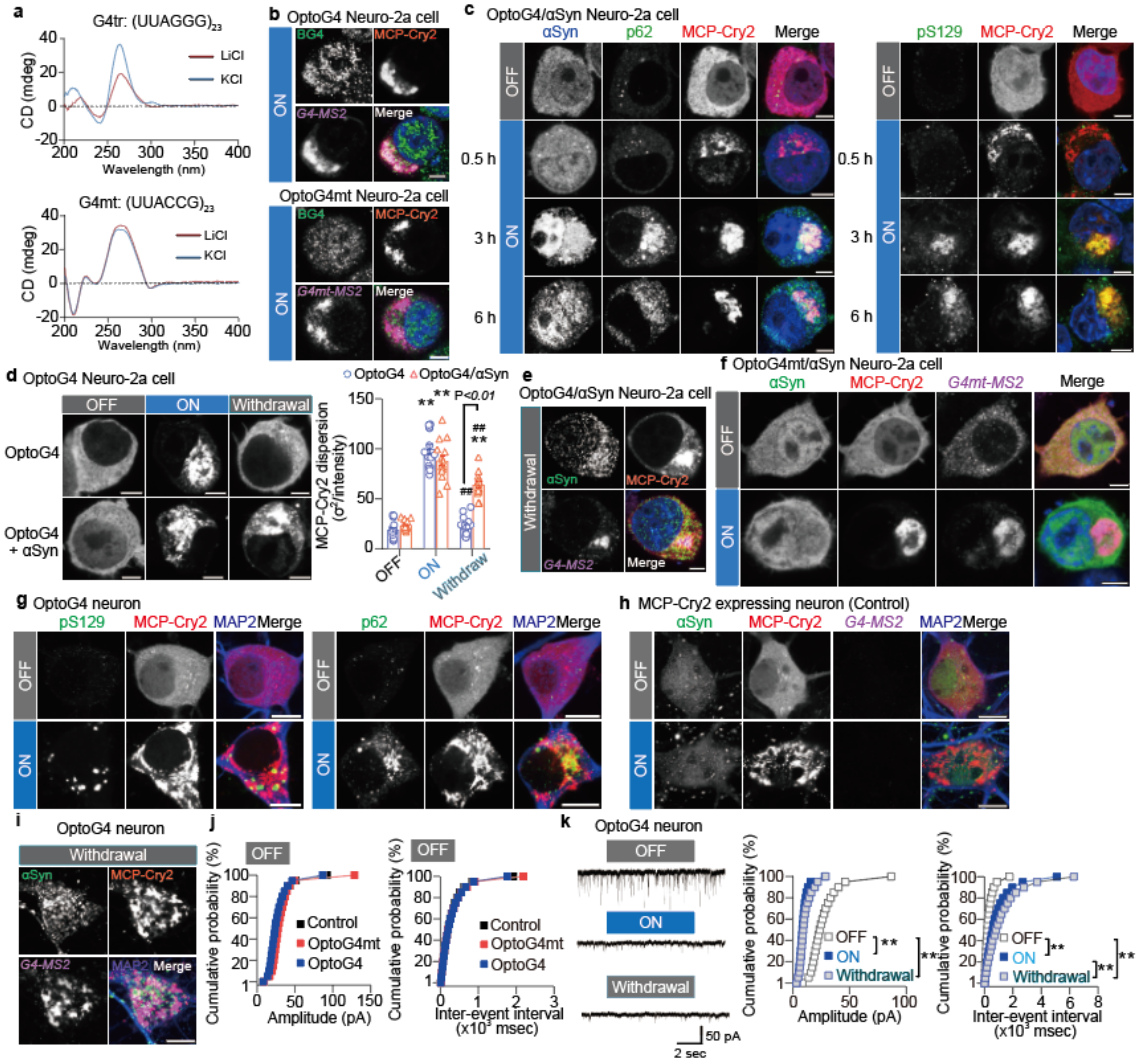

Extended Data Fig. 8: Establishment of forced RNA assembly in cells using optogenetics.

a, Circular dichroism spectra of G4tr $(UUAGGG)_{23}$ (left) and G4mt $(UUACCG)_{23}$ (right) in the presence of KCl or LiCl. **b**, Representative images of G4tr (top) or G4mt (bottom) assembly in OptoG4- (top) and OptoG4mt- (bottom) expressing Neuro-2a cells respectively, with 3-h BL stimulation. Scale bars, 5 μm. **c**, Representative images of p62 (left) and pS129 (right) in Neuro-2a cells co-expressing optoG4 and α-synuclein (αSyn) with blue light (BL) stimulation. Scale bars, 5 μm. **d**, Representative images (left) and quantification (right) of MCP-Cry2 dispersion in Neuro-2a cells co-expressing optoG4 and αSyn for 3 hours of BL stimulation followed by 3 hours of withdrawal. Scale bars, 5 μm. **e**, Representative images of co-assembly of αSyn (green) and *G4-MS2* RNA (magenta) in Neuro-2a cells co-expressing optoG4 and αSyn under the withdrawal condition. Scale bar, 5 μm. **f**, Representative images of Neuro-2a cells co-expressing optoG4mt and αSyn with 3-h BL stimulation. Scale bars, 5 μm. **g**, Representative images

of pS129 (left) and p62 (right) in optoG4-expressing mouse cultured neurons with 3-h BL stimulation. Scale bars, 5 μm. **h**, Representative images in MCP-Cry2-expressing mouse cultured neurons with BL stimulation for 3 h. Scale bars, 5 μm. **i**, Representative images of αSyn (green), MCP-Cry2 (red), *G4-MS2* RNA (magenta), and MAP2 (blue) in optoG4-expressing mouse cultured neurons under the withdrawal condition. Scale bar, 5 μm. **j**, Cumulative probability of sEPSCs related to **Fig. 4f** without BL stimulation. **k**, sEPSCs in OptoG4-expressing mouse cultured neurons for 3 hours of BL stimulation followed by 3 hours of withdrawal. Data are presented as mean ± standard error of mean. $^{**}P < 0.01$ vs. non-stimulated group and $^{\#\#}P < 0.01$ vs. stimulated group by one-way analysis of variance (ANOVA) with Bonferroni's multiple comparisons test (**d**). $^{**}P < 0.01$ by two-way ANOVA with Bonferroni's multiple comparisons test (**k**). Number of replicates is shown in Supplementary Table 9.

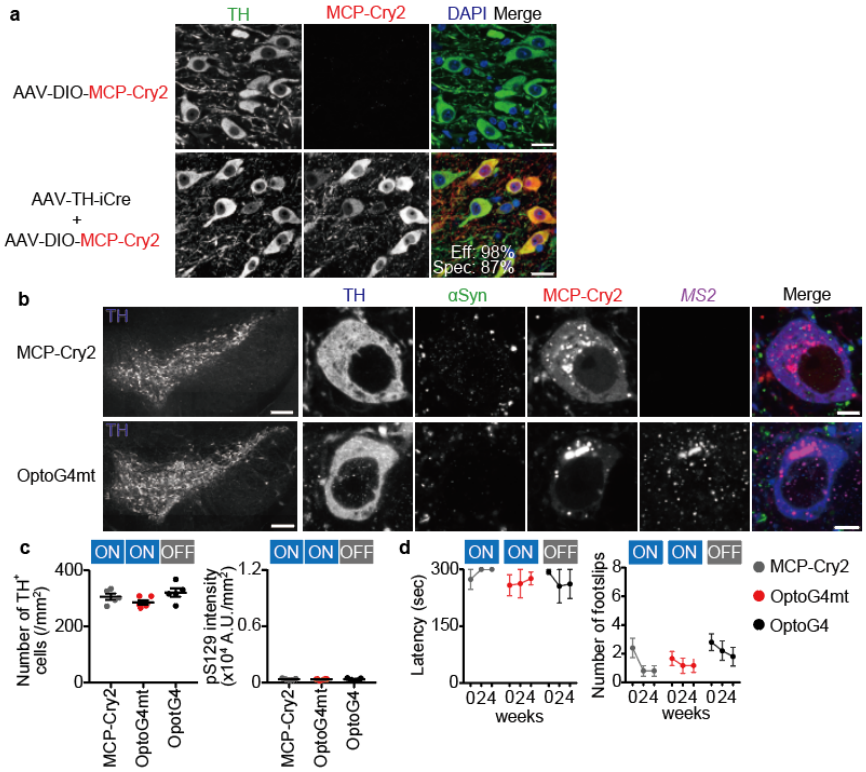

Extended Data Fig. 9: Forced RNA assembly in mouse nigral dopaminergic neurons by optogenetics.

a, Representative images of tyrosine hydroxylase (TH) (green), MCP-Cry2 (red), and 4',6-diamidino-2-phenylindole (blue) in the substantia nigra two weeks after the injection of AAV-DIO-MCP-Cry2 with AAV-pTH-iCre. Eff, efficiency; Spec, specificity. Scale bars, 20 µm. **b**, Representative images of TH (blue), αSyn (green), MCP-Cry2 (red), and *MS2* RNA (magenta) in the substantia nigra with blue light (BL) stimulation. Low and high magnification scale bars, 200 and 5 µm, respectively. **c**, Quantification of the number of TH-positive cells (left) and the fluorescent intensity of pS129 (right) in the substantia nigra with BL stimulation. **d**, Motor function in rotarod (left) and beam-walking (right) tasks with BL stimulation measured at the indicated time. Data are presented as mean ± standard error of mean. Number of replicates is shown in Supplementary Table 9.

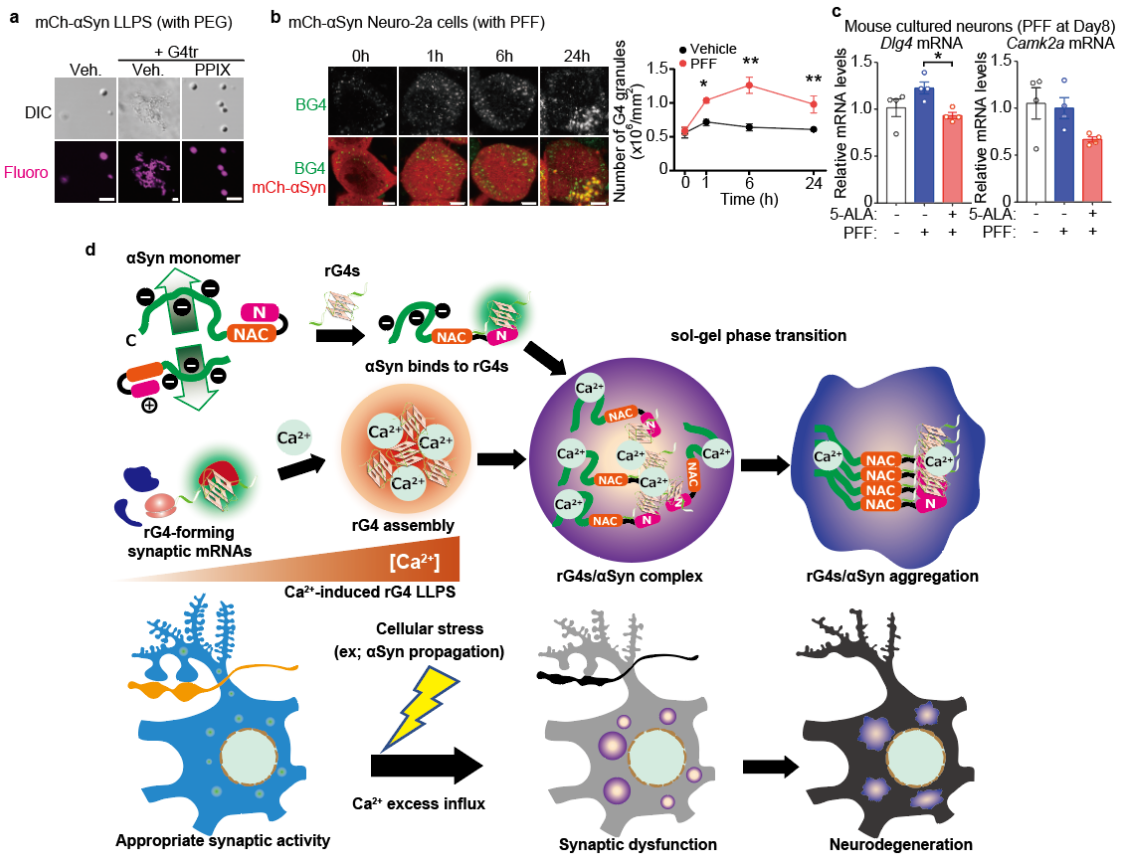

Extended Data Fig. 10: Effects of G4 ligand on RNA G-quadruplexes (rG4)-induced α-synuclein (αSyn) aggregation.

a, Representative images of *in vitro* phase-transitioned G4tr/αSyn dependent on polyethylene glycol) and the effect of protoporphyrin IX. Scale bars, 5 μm. **b**, Representative images (left) and quantification (right) of BG4 granules (green) of Neuro-2a cells expressing mCh-αSyn (red) followed by pre-formed fibril (PFF) treatment for the indicated time. Scale bars, 5 μm. **c**, *Dlg4* and *Camk2a* mRNA levels in mouse cultured neurons following PFF treatment and the effects of 3 μM 5-aminolevulinic acid (5-ALA). **d**, Schematic showing rG4 assembly-induced αSyn aggregation and neurodegeneration: The monomeric state of αSyn is maintained by biased electrostatic and hydrophobic intramolecular interactions and intermolecular repulsion. rG4s bind to N-terminus of αSyn directly and then promote its aggregation. In the presence of Ca^{2+}, enhanced rG4 assembly via liquid-liquid phase separation may serve as scaffolds for αSyn aggregation contributing to neurodegeneration. When neurons suffer from cellular stress such as αSyn propagation, αSyn aggregates with rG4 assembly composed of G4-forming synaptic mRNAs by Ca^{2+} excess influx, inhibiting synaptic protein translation, eliciting synaptic dysfunction, and eventually resulting in neurodegeneration. *$P < 0.05$ and **$P < 0.01$ by two-way (**b**) and one-way (**c**) analysis of variance with Bonferroni's multiple

1186 comparisons test. Number of replicates is shown in Supplementary Table 9.
1187

Supplementary Table 1. Enriched 12-mer sequences in αSyn and BG4 by MERMADE program.

Supplementary Table 2. BG4-enriched mRNAs in vehicle-treated mouse cultured neurons.

Supplementary Table 3. BG4-enriched mRNAs in pre-formed fibrils-treated mouse cultured neurons.

Supplementary Table 4. Prediction of G4 structure in BG4-enriched mRNAs in vehicle-treated mouse cultured neurons by quadruplex-forming guanine-rich sequences mapper.

Supplementary Table 5. Prediction of G4 structure in BG4-enriched mRNAs in pre-formed fibrils-treated mouse cultured neurons by quadruplex-forming guanine-rich sequences mapper.

Supplementary Table 6. Kyoto Encyclopedia of Genes and Genomes (KEGG) pathway analysis in BG4-enriched mRNAs in vehicle-treated neurons.

Supplementary Table 7. Kyoto Encyclopedia of Genes and Genomes (KEGG) pathway analysis in BG4-enriched mRNAs in pre-formed fibrils-treated neurons.

Supplementary Table 8. Gene Ontology (GO) analysis in BG4-enriched mRNAs in pre-formed fibrils-treated neurons.

Supplementary Table 9. Statistical analysis and number of replicates.

Supplementary Method.

Supplementary Video. Live imaging of pre-formed fibrils (PFF)-treated cells following GFP-α-synuclein (αSyn) expression in a fluorescence recovery after photobleaching (FRAP) assay.

FRAP assay in HEK293T cells-expressing GFP-αSyn treated with PFF for the indicated time. Scale bars, 2 μm. Open circles in green indicate the regions of photobleaching.